FAKULTÄT FÜR PHYSIK
Institut für Experimentelle Kernphysik

Optimization of the KATRIN rear wall for a keV-scale sterile neutrino search

Bachelorarbeit
von

Ellen Förstner

am Institut für Experimentelle Kernphysik

Erstgutachter:	Prof. Guido Drexlin, IEKP, KIT
Zweitgutachter:	Prof. Susanne Mertens, MPI, TUM
Betreuer:	Anton Huber, IEKP, KIT
	Marc Korzeczek, IEKP, KIT

Bearbeitungszeit: 02.05.2016 – 31.01.2017

Erklärung zur Selbstständigkeit

Ich versichere, dass ich diese Arbeit selbstständig verfasst habe und keine anderen als die angegebenen Quellen und Hilfsmittel benutzt habe, die wörtlich oder inhaltlich übernommenen Stellen als solche kenntlich gemacht und die Satzung des KIT zur Sicherung guter wissenschaftlicher Praxis in der gültigen Fassung vom 17.05.2010 beachtet habe.

Karlsruhe, den 31.01.2017, _____

Ellen Förstner

Als Ansichtsexemplar genehmigt von

Karlsruhe, den 31.01.2017, _____

Prof. Guido Drexlin, IEKP, KIT

Introduction and Objectives

The nature of dark matter is one of the greatest questions for physics of our time. A sterile neutrino in the keV mass range is a favored dark matter candidate. These neutrinos could act as warm dark matter and are in good agreement with cosmological observations. As the right handed equivalent of the active neutrino states, they are only a small extension to the standard model.
In Karlsruhe the **KA**rlsruhe **TRI**itium **N**eutrino (KATRIN) experiment was designed and built to measure the overall mass scale of the active neutrino states, first data taking will start in the future [KAT05]. The neutrino mass is determined by measuring the endpoint region of the tritium β-decay spectrum. KATRIN will reach a sensitivity of 0.2 eV (90% CL) [KAT05]. The experimental setup holds a great potential to be also used for a sterile neutrino search [D$^+$16]. Most of all the source with its luminosity, creating up to 10^{11} β-decay electrons per second, and the spectrometer with an extremely high energy resolution of 0.93 eV [KAT05].
Through mixing of active and sterile states the tritium β-decay spectrum gets distorted and a kink can be found at an energy of

$$E_{\text{kink}} = E_0 - m_s,$$

E_0 being the endpoint energy of the β-decay spectrum and m_s the mass of the sterile neutrino state. To detect this distortion the tritium spectrum needs to be measured with great precision. Hence all systematic effects, that mimic such a distortion of the spectrum must be suppressed to very low scales or modeled with high precision.
One of these effects is the scattering of electrons on the gold rear wall of the KATRIN experiment. In the following thesis, this effect is investigated in detail, using monte carlo simulations, and different possible countermeasures are considered. To do so, the influence of the position, material and the magnetic field at the rear wall was taken into account in the study. To this end, 1) electron backscattering and secondary electron production at the rear wall, as well as 2) the propagation of electrons to and from the rear wall was simulated with GEANT4 and KASPER, respectively. The influence of the three parameters (magnetic field, position and material) was systematically investigated (see chapter 2).
Out of the list of possible countermeasures five different settings are studied. As a final result, the best setting, with the highest suppression, is presented.

Einleitung und Zielsetzung

Die Natur der dunklen Materie ist eine der größten Fragen für die Physik unserer Zeit. Ein steriles Neutrino im keV-Massenbereich ist ein möglicher dunkle Materie Kandidat. Diese Neutrinos könnten als warme dunkle Materie fungieren und sind in guter Übereinstimmung mit kosmologischen Beobachtungen. Als rechtshängiges Äquivalent zu den aktiven Neutrino-Zuständen sind sie nur eine geringe Erweiterung des Standardmodells.
Das **KA**rlsruhe **TRI**itium **N**eutrino-Experiment (KATRIN) wird entworfen und gebaut, um die Gesamtmassenskala der aktiven Neutrinozustände zu messen, die erste Datennahme soll in naher Zukunft beginnen [KAT05]. Die Bestimmung der Neutrinomasse erfolgt durch Vermessung der Endregion des Tritium-β-Zerfallsspektrums. KATRIN wird eine Sensitivität von 0.2 eV (90% CL) erreichen [KAT05]. Die Versuchsanordnung besitzt großes Potential, auch für eine Suche nach sterilen Neutrinos im keV-Massenbereich verwendet zu werden [D$^+$16]. Vor allem die Quelle, die mit ihrer Luminosität bis zu 10^{11} β-Elektronen pro Sekunde produziert und das Spektrometer mit extrem hoher Energieauflösung von 0.93 eV [KAT05] sind prädestiniert.
Durch die Mischung von aktiven mit sterilen Zuständen wird das Tritium-β-Spektrum verzerrt und ein Knick bildet sich bei einer Energie von

$$E_{\text{Knick}} = E_0 - m_s.$$

E_0 ist die Endpunktsenergie des β-Spektrums und m_s die Masse des sterilen Neutrino-Zustands. Um diese Verformung des Spektrums zu analysieren, muss das Spektrum mit großer Genauigkeit vermessen werden. Daher müssen alle systematischen Effekte, die eine solche Verformung des Spektrums verursachen, sehr stark unterdrückt, oder im Detail beschrieben werden.
Einer dieser Effekte ist die Streuung von Elektronen an der Goldrückwand des KATRIN Experiments. In der folgenden Arbeit wird dieser Einfluss mit Hilfe von Monte-Carlo-Simulationen im Detail untersucht und verschiedene mögliche Methoden zur Unterdrückung in Betracht gezogen. Dabei wurde der Einfluss der Position, des Materials und des Magnetfeldes an der Rückwand berücksichtigt. Die Erzeugung von Sekundärelektronen spielt dabei ebenfalls eine Rolle. Ein komplettes Spektrum der gestreuten Elektronen, unter Berücksichtigung der Produktion von Sekundärteilchen, wurde simuliert ebenso wie seine Propagation zum Detektor. Der Einfluss der drei Parameter (Magnetfeld, Position und Material) wurde systematisch überprüft (siehe Kapitel 2).
Aus der Liste der möglichen Gegenmaßnahmen wurden fünf verschiedene Szenarien untersucht. Am Ende wird die beste Einstellung, mit der höchsten Unterdrückung vorgestellt.

Contents

Introduction and Objectives v

Einleitung und Zielsetzung vii

1. Neutrino mass measurement and search for keV-scale sterile neutrinos with KATRIN 1
- 1.1. Neutrino Physics . . . 1
  - 1.1.1. History of the Neutrino . . . 1
  - 1.1.2. Sterile Neutrino and Dark Matter . . . 3
- 1.2. The KArlsruher TRItium Neutrino Experiment (KATRIN) . . . 4
  - 1.2.1. KATRIN measurement principle . . . 4
  - 1.2.2. KATRIN Main Components . . . 6
  - 1.2.3. Sterile neutrino search with the KATRIN setup . . . 8

2. The rear wall as a systematic effect for a keV-scale sterile neutrino search 11
- 2.1. Staged approach for a keV-scale sterile neutrino search . . . 11
- 2.2. The KATRIN setup for the phase-0 measurement . . . 12
- 2.3. Backscattered and Auger electrons from the rear wall . . . 13
- 2.4. Countermeasures . . . 14

3. Results of the Thesis 19
- 3.1. Discussed scenarios . . . 19
- 3.2. Simulation Method . . . 20
  - 3.2.1. KASPER simulations . . . 20
  - 3.2.2. GEANT4 simulations . . . 26
- 3.3. Analysis of simulation results . . . 27
  - 3.3.1. Results for scenario 1 . . . 31
  - 3.3.2. Result for scenario 2 . . . 32

4. Conclusion 37

Appendix 39
- A. KASPER simulations . . . 39
  - A.1. Calculation of the safety margin for Au-high . . . 39
  - A.2. Parameters and results for other scenarios . . . 39
- B. GEANT4 simulations . . . 42
  - B.1. Summary of all results . . . 42
  - B.2. Validation of the GEANT4 monte carlo simulation toolkit . . . 42

Bibliography 55

List of Figures

1.1. Neutrino Mass Scenarios . . . 3
1.2. Tritium spectrum for neutrino mass unequal zero . . . 4
1.3. MAC-E filter working principle . . . 6
1.4. Overview of the KATRIN setup . . . 7
1.5. Tritium spectrum with the kink of a sterile neutrino . . . 8

2.1. Rear wall chamber with gold rear wall . . . 12
2.2. Magnetic setup in phase-0 mode - Scenario 1 . . . 13
2.3. Backscattering of electrons . . . 14
2.4. Production of Auger electrons . . . 15
2.5. Acceptance angle and transmission probability . . . 16
2.6. Backscattering on gold for different impact angles . . . 17
2.7. Backscattering on different materials . . . 18
2.8. Rear wall chamber with beryllium rear wall . . . 18

3.1. Discussed scenarios . . . 20
3.2. Geometry of KASPER simulations . . . 22
3.3. Au-high: electron trajectories in rear wall chamber . . . 23
3.4. Au-high: magnetic field at rear wall . . . 24
3.5. Scenario2: electron trajectories in rear wall chamber . . . 24
3.6. Scenario2: magnetic field at rear wall . . . 25
3.7. GEANT4 simulation geometry . . . 26
3.8. GEANT4: Input tritium spectrum . . . 27
3.9. Au-high: Backscatter spectrum at rear wall and influence of Auger processes 28
3.10. Processing of simulation results . . . 30
3.11. Au-high: Spectrum at detector including backscattering . . . 31
3.12. Au-high: Ratio plot . . . 32
3.13. Au-low: Spectrum at detector including backscattering . . . 33
3.14. Be-high: Spectrum at detector including backscattering . . . 33
3.15. Be-low: Spectrum at detector including backscattering . . . 34
3.16. Scenario 2: Spectrum at detector including backscattering . . . 34

A.1. Au-low: electron trajectories in rear wall chamber . . . 40
A.2. Au-low: magnetic field at rear wall . . . 41
A.3. Be-high: electron trajectories in rear wall chamber . . . 41
A.4. Be-high: magnetic field at rear wall . . . 42
A.5. Be-low: Electron trajectories in rear wall chamber . . . 42
A.6. Be-low: magnetic field at rear wall . . . 43
B.7. Au-low: Spectra at detector and ratio plot . . . 44
B.8. Be-high: Spectra at detector and ratio plot . . . 45
B.9. Be-low: Spectra at detector and ratio plot . . . 46
B.10. SS-low: Spectra at detector and ratio plot . . . 47

B.11.SS-high: Spectra at detector and ratio plot 48
B.12.Scenario 2: Spectra at detector and ratio plot 49
B.13.Energy spectrum with Auger lines 50
B.14.Auger lines for gold nano-particles 51
B.15.Comparison of reproduced simulation to data from [I$^+$16] 53

List of Tables

3.1. Values from KASPER simulations 25
3.2. Results from GEANT4 simualtions 35

1. Neutrino mass measurement and search for keV-scale sterile neutrinos with KATRIN

1.1. Neutrino Physics

Neutrinos knowingly possess the smallest mass among all known massive standard model (SM) particles. They only interact via the weak interaction and are therefore difficult to detect. Not without reason they carry the nickname 'ghost particles'.

1.1.1. History of the Neutrino

Despite the fact that they are essential for numerous leptonic interactions, it took some time to postulate neutrinos and finally proof their existence. The following section describes the different steps that led to our todays knowledge about neutrinos.

Discovery of the neutrinos

1930 W. Pauli postulated the neutrino to explain the continuous energy spectrum of β-decay electrons [Pau30]. Without the existence of an additional particle, β-decay would be a two body decay where a proton decays into a neutron and therefore mono-energetic electrons are expected. In his letter addressed to the 'Radioaktiven Damen und Herren' [Pau30] Pauli first called his new particle neutron since the particle has no electrical charge. After the discovery of the neutron as a counter part to the proton the today's name 'neutrino' was introduced by E. Fermi. He also developed a theoretical foundation for β-decay that made use of the new particle [Fer34]. Fermi's Golden Rule describes the transition probability $\lambda_{i\to f}$ of the mother to the daughter nucleus, and depends on the coupling strength between final and initial state described by the matrix element $M_{i\to f}$ and the density of final states ρ_f:

$$\lambda_{i\to f} = \frac{2\pi}{\hbar} \left|M_{i\to f}\right|^2 \rho_f. \tag{1.1}$$

It took another 22 years before in 1956 Reines and Cowan proved the existence of the neutrino (more precisely of the electron anti-neutrino) with their 'poltergeist project' [CRH+56]. In a tank filled with water and solved cadmium chloride electron anti-neutrinos $\bar{\nu}_e$ (from a reactor) react with the protons (hydrogen nuclei) via inverse β-decay:

$$\bar{\nu}_\mathrm{e} + \mathrm{p} \longrightarrow \mathrm{n} + \mathrm{e}^+. \tag{1.2}$$

The produced positron quickly annihilates with an electron, emitting two photons. After moderation of the neutron due to scattering with protons it reacts with the cadmium via

$$\mathrm{n} + {}^{113}\mathrm{Cd} \longrightarrow {}^{114}\mathrm{Cd} + \gamma\,. \tag{1.3}$$

Consequently additional photons are produced a few microseconds after the first two.
The detection of these characteristic two light signals shortly after one another proved the existence of the neutrino.
In 1962 the muon neutrino was not only discovered but also identified as an additional flavor state [D$^+$62]. This means decays such as

$$\nu_\mu + \mathrm{p} \longrightarrow \mathrm{e}^- + \mathrm{p} \tag{1.4}$$

are not observed since the neutrino in the muon flavor is unable to interact with the electron.
When the τ lepton was found in 1975 it only seamed natural to assume the existence of a tau neutrino. Again its detection took several years. In 2000 the DONUT experiment (Fermilab) succeeded in this task of finding the last missing SM fermion [K$^+$01].
Generally in the SM neutrinos are considered as massless. However following investigations should disagree with this assumption.

Neutrino oscillations

The Homestake-Experiment starting in the 1960s under the lead of Davis and Bahcall was the first to detect solar neutrinos [Dav94]. They were detected in a tank filled with tetrachloroethylene via a charged-current interaction:

$$^{37}\mathrm{Cl} + \nu_\mathrm{e} \longrightarrow {}^{37}\mathrm{Ar} + \mathrm{e}^+. \tag{1.5}$$

The capture of a ν_e was proved by detecting the Argon atoms.
However only about 1/3 of the expected neutrino flux, resulting from the Standard Solar Model (SSM) [BPB01], was detected. An incorrect experimental setup as well as the falseness of the SSM were discussed as an explanation for the results.
However the SNO-experiment starting their measurements in 1999 could verify the results from Homestake [A$^+$01]. Here a tank filled with heavy water (D_2O) served as a Cherenkov detector to detect electrons resulting from the solar neutrino reactions:

$$\begin{aligned} \nu_\mathrm{e} + \mathrm{D} &\longrightarrow \mathrm{e}^- + \mathrm{p} + \mathrm{p} \quad \text{charged-current,} \\ \nu_\mathrm{x} + \mathrm{D} &\longrightarrow \nu_\mathrm{x} + \mathrm{p} + \mathrm{p} \quad \text{neutral-current,} \\ \nu_\mathrm{x} + \mathrm{e}^- &\longrightarrow \nu_\mathrm{x} + \mathrm{e}^- \quad \text{elastic scattering.} \end{aligned} \tag{1.6}$$

Charged-current reactions are only sensitive to ν_e and also just registered 1/3 of the expected flux from the sun. Neutral-current reactions and elastic scattering are sensitive to all neutrino flavors. The rate of neutrinos detected via these channels corresponded to the SSM predictions.
The only reasonable explanation for this results was to assume that neutrinos oscillate and change their flavor during propagation, as first suggested by Pontecorvo [Pon58].
Parallel, atmospheric neutrino experiments came to the same conclusion. With the water-cherenkov-detector of the Super-Kamiokande experiment both flavor (ν_e or ν_μ) and direction of an incoming atmospheric neutrino could be measured [F$^+$98]. These neutrinos origin from hadron cascades in earths atmosphere.
This experiment revealed that the ratio N_{ν_e}/N_{ν_μ} depended on the zenith angle. Neutrinos traversing the earth before reaching the detector, were detected with $N_{\nu_e}/N_{\nu_\mu} = 0.5$ whereas one would expect $N_{\nu_e}/N_{\nu_\mu} = 0.3$ for neutrinos originating from the atmosphere [F$^+$98]
Again neutrino oscillation was the best theory to explain the results.

Theoretical description of neutrino oscillations

Oscillation of neutrinos makes it possible to measure a neutrino with a different flavor than the one it was created with. Their flavor eigenstate (interaction) is different to their mass

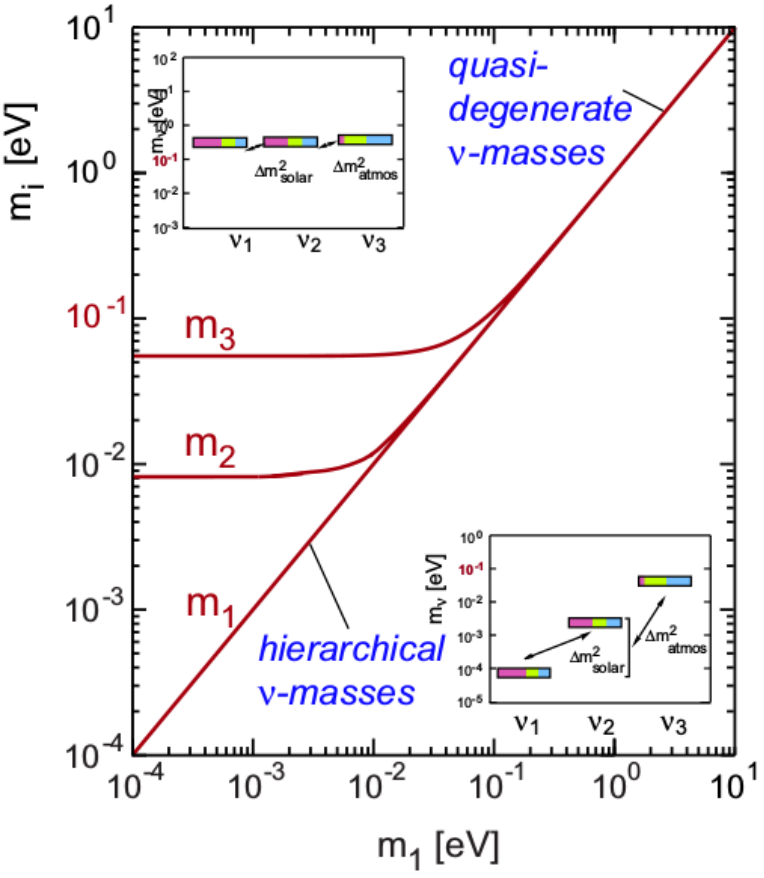


Figure 1.1.: With the knowledge of the total mass-scale of neutrinos it would be possible to distinguish whether the mass eigenstates ν_1, ν_2 and ν_3 (above labled as m_{1-3}) are hierarchical (left side) or quasi-degenerate (right side). Figure from [KAT05]

eigenstate (propagation). Therefore flavor eigenstates (ν_e, ν_μ, ν_τ) and mass eigenstates (ν_1, ν_2, ν_3) are distinguishable.
A neutrino of a certain flavor, interacting via weak interaction, is always a superposition of the three mass eigenstates. The mixing is described through the mixing matrix U:

$$\begin{pmatrix} \nu_e \\ \nu_\mu \\ \nu_\tau \end{pmatrix} = \mathrm{U} \cdot \begin{pmatrix} \nu_1 \\ \nu_2 \\ \nu_3 \end{pmatrix} \tag{1.7}$$

Flavor oscillation requires different mass eigenstates $\nu_1 \neq \nu_2 \neq \nu_3$ therefore not all neutrino masses can be zero. Neutrino oscillation only depends on the mass difference of two states. These differences can be accessed with oscillation experiments. The absolute mass scale however, has to be determined in another way. This total mass scale is very interesting for the understanding of physics beyond the SM. Knowledge of the total mass scale of neutrinos would allow to determine whether their mass states are hierarchical ($\nu_1 \ll \nu_2 \ll \nu_3$) or quasi-degenerate ($\nu_1 \approx \nu_2 \approx \nu_3$, see figure 1.1).

1.1.2. Sterile Neutrino and Dark Matter

Also cosmology is very interested in knowing the contribution Ω_ν of neutrinos to the total amount of dark matter (DM). As of today only three light mass eigenstates were considered. However additional mass eigenstates are imaginable. Such a neutrino would mostly be 'sterile' and could only interact via its tiny admixture to active flavors.
This thesis focuses on sterile neutrinos in the keV mass range. Such a neutrino is a favored

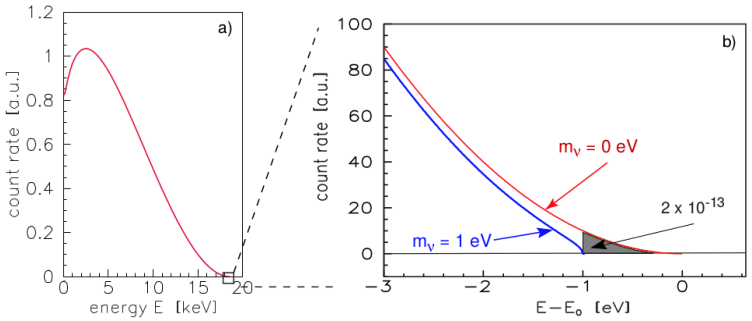


Figure 1.2.: For a non-vanishing neutrino mass (blue line) the endpoint region (right side) of the tritium β-decay spectrum (left side) is shifted to lower energies. Even for a neutrino at rest some energy is needed to create its mass. Therefore the electron can not possess all during decay released energy. The maximum electron energy is lower compared to the spectrum with a neutrino mass of 0 eV (red line). Figure from [KAT05].

DM candidate. Within this mass range a sterile neutrino could act as warm dark matter and is in agreement with cosmological observations [DW94].
Astrophysical observations constrain the possible parameter space (mass and mixing angle[1] θ) of a sterile neutrino [BIR12]:

$$\begin{aligned} 1\,\text{keV} < & m_s < 50\,\text{keV} \\ 10^{-13} < & \sin^2(2\theta) < 10^{-7} \end{aligned} \tag{1.8}$$

As described in the next section the KATRIN-Experiment holds the possibility of searching for keV-scale sterile neutrinos, and could be capable of reaching into the not excluded parameter space.

1.2. The KArlsruher TRItium Neutrino Experiment (KATRIN)

KATRIN is a next-generation single β-decay experiment with the aim of determining the total neutrino mass scale. After three years of measurement it will reach a sensitivity of 0.2 eV (90% CL) [KAT05].
In this chapter the KATRIN experiment, including the measurement principle and its main components, is introduced as described in the KATRIN Design Report 2004 [KAT05].
The advantages and challenges of KATRIN with respect to a keV-scale sterile neutrino search will be discussed at the end of this section.

1.2.1. KATRIN measurement principle

KATRIN uses a model-independent way to measure the neutrino mass. The released energy in a β-decay is split between the daughter nucleus, electron and neutrino in a quantum mechanical process. Therefore the electron can possess various different energies up to the endpoint energy of the decay (β-decay spectrum). However as the neutrino has a rest mass unequal zero the electron can never posses all the released β-decay energy since a certain amount of energy is needed to create the electron-anti-neutrino. This results in a deformation of the energy spectrum with the biggest manifestation in the endpoint region as shown in figure 1.2.
At KATRIN the endpoint region of the β-decay spectrum from molecular tritium in equation 1.9 is measured with high precision. With only basic corrections like the Coulomb interaction

[1] The mixing angle describes how much a certain mass-eigenstate contributes to a particular flavor eigenstate.

of the electron with the nucleus, expressed through the Fermi-function $F(E, Z = 2)$, the β-spectrum is given by [M+15]:

$$\frac{\mathrm{d}\Gamma}{\mathrm{d}E} \propto F(E, Z = 2) \cdot p \cdot (E + m_e) \cdot (E_0 - E) \cdot \sqrt{(E_0 - E)^2 - m^2_{\nu,\mathrm{eff}}}. \tag{1.9}$$

E and m_e are energy and mass of the electron, E_0 is the endpoint energy with a neutrino mass of zero. Because the difference between different mass eigenstates is so small and can not be resolved with the KATRIN sensitivity an effective neutrino mass $m_{\nu,\mathrm{eff}}$ is used. Tritium holds many characteristics that make it an ideal candidate for β-decay experiments. A short half life of 12.3 years and a low endpoint energy of 18.6 keV make it possible to get the high count rates needed to produce enough electrons in the endpoint region of the spectrum. Its simple molecular and electron shell structure allows comparatively simple corrections for the interaction of β-decay electrons with the daughter nuclei. Also tritium remains gaseous even at very low temperatures allowing to have a very stable cryogenic source [KAT05].
Molecular tritium decays into a helium ion (molecular bound to a tritium atom), an electron and an electron anti-neutrino

$$\mathrm{T_2} \longrightarrow \mathrm{THe^+} + \mathrm{e^-} + \bar{\nu}_\mathrm{e}. \tag{1.10}$$

The MAC-E filter principle

The heart of KATRIN is its spectrometer, that works with the Magnetic-Adiabatic-Collimation combined with an Electrostatic Filter (mac-e filter) principle. This mac-e filter allows very high energy resolution [KAT05].
The electrons are guided in cyclotron trajectories along magnetic field lines created by two solenoids on either sides of the spectrometer vessel. At their creation, β-decay electrons possess various different angles relative to the magnetic field, splitting their kinetic energy E_tot in a component parallel to the field $E_\parallel$ and a component transversal to the field $E_\perp$

$$E_\mathrm{tot} = E_\parallel + E_\perp. \tag{1.11}$$

From the upstream end to the middle of the spectrometer (analyzing plane) the magnetic field drops by many orders of magnitude resulting in the transformation of cyclotron energy into longitudinal motion [KAT05]. This change from isotropically emitted electrons into a beam with momenta parallel to the magnetic field is depicted in figure 1.3.
On the way to the analyzing plane the electrons propagate towards an electrostatic retarding potential (maximum strength at the lowest magnetic field). Only those with a high enough longitudinal kinetic energy will pass the middle of the spectrometer vessel, and are able to reach the detector.
The spectrometer acts as an integrating high-pass filter, letting all electrons with energies higher than the spectrometer potential pass. Its energy resolution depends on the magnetic field in the center of the spectrometer $B_A = 3\,\mathrm{G}$ [KAT05] and the highest field between source and detector $B_\mathrm{max} = 6\,\mathrm{T}$:

$$\frac{\Delta E}{E} = \frac{B_A}{B_\mathrm{max}} \quad \Rightarrow \quad \Delta E(E = 18.6\,\mathrm{keV}) = \frac{3\,\mathrm{G}}{6\,\mathrm{T}} \cdot 18.6\,\mathrm{keV} = 0.93\,\mathrm{eV}. \tag{1.12}$$

Magnetic reflection

Momentum transformation in a varying magnetic field can also lead to reflection or trapping of particles. Magnetic reflection will play a central role in this thesis.
If an electrons propagates along an increasing magnetic field the angle between momentum and magnetic field also increases. When 90° are reached and the field rises even more the

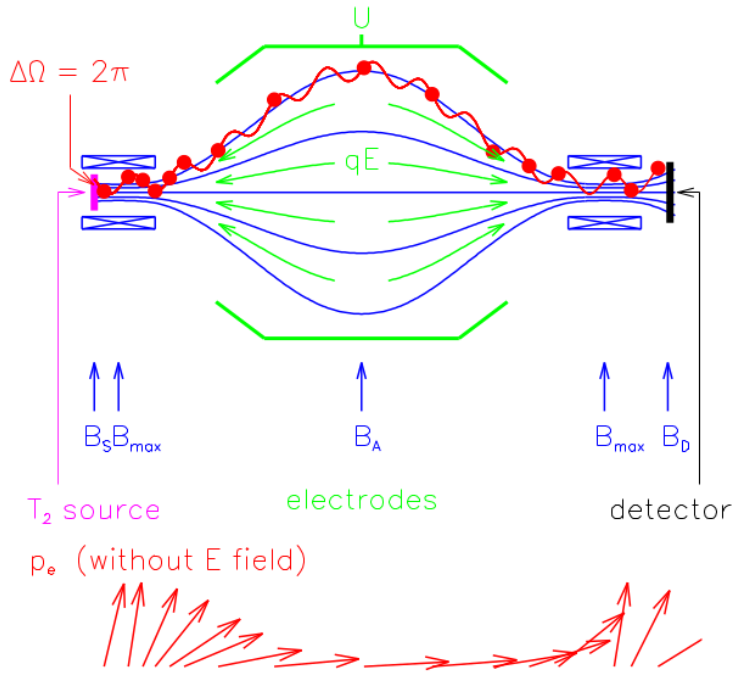


Figure 1.3.: Spectrometer vessel with solenoids on either side generating a magnetic field (in blue) with a minimum field strength in the analyzing plane (center of vessel B_{A}). The retarding (and re-accelerating) electric field is shown in green. The momentum arrow at the bottom resembles the transformation of cyclotron energy in longitudinal motion caused by the decreasing magnetic field (electric retarding potential turned off). Figure from [KAT05].

momentum 'flips over' and the electrons moves in the opposite direction (reflection). Whether or not the electron is reflected depends on the difference of the initial and highest magnetic field within the electron trajectory and on the initial angle of the electron between it's momentum and the initial magnetic field B_{ini}. To cross the magnetic barrier the angle needs to be below a certain acceptance angle

$$\Theta_{\mathrm{max}} = \arcsin\left(\sqrt{\frac{B_{\mathrm{ini}}}{B_{\mathrm{max}}}}\right). \tag{1.13}$$

1.2.2. KATRIN Main Components

All together the KATRIN setup shown in figure 1.4 has a length of 70 m with a magnetic flux of 191 T cm^2 [KAT05] in which tritium β-decay electrons are guided from the source to the detector.

WGTS

β-decay electrons are produced in the windowless gaseous tritium source (WGTS) through the decay of gaseous molecular tritium (see equation 1.10). In a magnetic field of 3.6 T tritium with a purity of more than 95% and a temperature of 27 K is injected in the middle of the source tube and diffuses to both ends [KAT05]. There it is pumped out by sets of turbo molecular pumps of the differential pumping section (DPS), cleared and enriched in a closed tritium loop and injected again. A column density of 5×10^{17} molecules/cm^2 leads to 10^{11} decays per second [KAT05]. The electrons are emitted isotropically and are guided along magnetic field lines both towards transport and rear section.

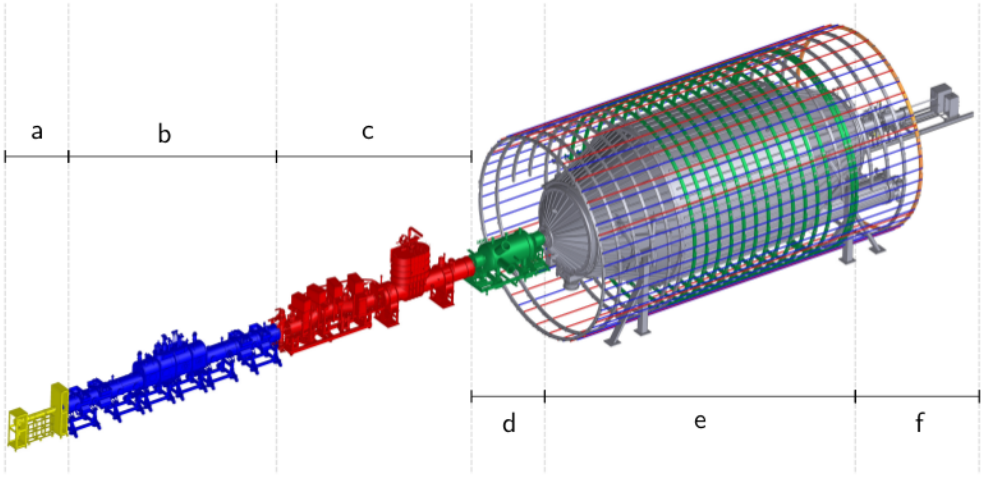


Figure 1.4.: KATRIN setup with a total length of 70 m. Its main components are (from left ot right) the rear rection (a), tritium source (b), transport section with DPS and CPS (c), pre- and main spectrometer (d and e) and the detector section (f). Figure from [Kle14].

Rear Section

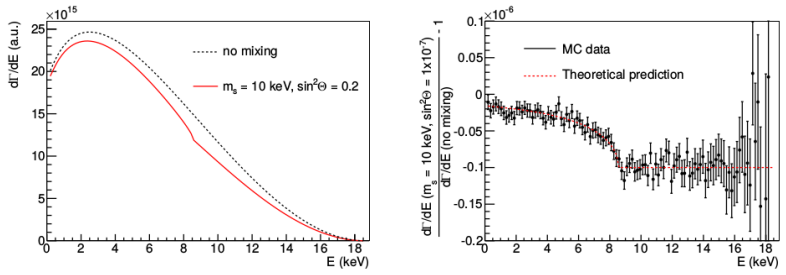
The rear section (RS) is located on the upstream end of the WGTS. It contains the calibration and monitoring system (CMS) with a rear detector used to monitor the source activity and an electron gun (E-Gun) used to measure the overall response of the KATRIN setup [KAT05].
Since the rear wall and rear wall chamber, parts of the RS, play a central role in this thesis they will be discussed in detail in chapter 2.

Transport Section

All electrons from the WGTS that do not propagate towards the RS make their way through the transport section towards the spectrometer and detector. The main task of the transport section is the reduction of the tritium and helium-ion particle pressure. This is very important since the tritium/helium particles would cause a significant background when they enter the spectrometer section.
While the electrons are guided along strong magnetic fields through this section, tritium faces a variety of barriers resulting in a suppression of the tritium flow of 14 orders of magnitude from source to spectrometer pressure [KAT05].
The active differential pumping section (DPS), consisting of multiple turbo molecular pumps in the rear and front of the WGTS, extracts most of the tritium. A bend in the beam tube lets tritium hit the walls while electrons are guided around them.
Any tritium left faces the passive cryogenic pumping section (CPS). The beam tube is cooled down to a temperature of 4.5 K [KAT05] whereby the tritium is absorbed in the attached argon frost. Again chicanes in the beam tube support the extraction of tritium.

Spectrometers

In both pre- and main spectrometer an ultra-high vacuum of less than 10^{-11} mbar is generated in a volume of 1400 m^3 [KAT05]. The energy measurement is based on the MAC-E filter principle described in the previous section.
The pre-spectrometer located upstream of the main spectrometer rejects all low-energy electrons and was used as a test facility before the construction of the main spectrometer.



(a) (b)

Figure 1.5.: a: β-spectrum without (black line) and with the imprint of a sterile neutrino (red line). Here the unrealistic case of a mixing-angle of $\sin^2\theta = 0.2$ is shown. b: An easy way to make the kink more visible is to look at the ratio of a spectrum with and without kink. Figure from [M+15].

With a diameter of about 10 m the main spectrometer is much larger than the pre-spectrometer and reaches an energy resolution of 0.93 eV (see equation 1.12) [KAT05]. Downstream of the main spectrometer the pinch-magnet is located. Its magnetic field of 6 T is the highest of the whole setup [KAT05].

Detector

At the end of the setup electrons that passed the spectrometers reach 63 cm^2 of circular sensitive detector area [KAT05]. The Focal-Plane Detector (FPD) consists of PIN diodes and is segmented into 148 pixels to enable position sensitivity [Har12].

1.2.3. Sterile neutrino search with the KATRIN setup

Due to its excellent source and spectrometer properties, KATRIN can extend its physics reach from measuring the neutrino mass to searching for sterile neutrinos. A sterile neutrino would manifest itself in the shape of the tritium spectrum, since the mixing with the active neutrino states leads to an additional term in equation 1.9. The β-spectrum then consists of two contributions [M+15]:

$$\frac{\mathrm{d}\Gamma}{\mathrm{d}E} = \cos^2\theta \frac{\mathrm{d}\Gamma}{\mathrm{d}E}(m_a) + \sin^2\theta \frac{\mathrm{d}\Gamma}{\mathrm{d}E}(m_s). \tag{1.14}$$

Where θ is the active-sterile-mixing angle. The active neutrino mass m_a is much smaller than the sterile neutrino mass m_s ($m_s \ll m_a \approx 0$). Because of its great mass the sterile neutrino spectrum has a much lower endpoint energy. This leads to a 'kink' in the spectrum. As can be seen in figure 1.5 the signature of a sterile neutrino is further away from the endpoint. To be able to cover a possible broad range of the keV-scale sterile neutrino parameter space, the whole tritium β-decay spectrum is of interest [M+15].

The KATRIN setup holds many advantages for a keV-scale sterile neutrino search.
Due to its high luminosity and stability, the KATRIN WGTS is of great advantage for a search for keV-scale sterile neutrinos. Especially its possibility to function without a membrane to prevent tritium from entering the spectrometer thanks to the effective tritium containment system with DPS and CPS. Even the small energy loss an electron would experience by passing the membrane would have a great impact in the lower energy ranges of the spectrum. Also the very high energy resolution of the spectrometer benefits a sterile neutrino search.
Since KATRIN is optimized to measure only the endpoint region of the β-spectrum many new challenges occur when you use KATRIN to measure deeper into the tritium β-decay spectrum. Systematic effects that cause an energy loss of electrons or create additional low energy electrons do not play a role in the KATRIN measurement since all these electrons

are rejected in the spectrometer. When measuring the entire spectrum they have a great impact especially in lower energy ranges [B$^+$16].
Another challenge occurs at the detector. For low spectrometer potentials many electrons reach the detector(up to 10^{11} cps). It is however not designed for such high count rates, as only very few cps are in the region of interest for the neutrino mass determination. Hence the most important challenge is to ensure low enough detector count rates, not exceeding of the order of 10^5 cps [B$^+$16], when measuring the low energy ranges of the β-decay spectrum. To lower the rate for a search for keV-scale sterile neutrinos, a lower source strength or a low source field can be used.
Less tritium in the source leads to a lower overall count-rate. But the pressure in the source can not be lowered unlimited, since for low source pressures the stability (constant pressure in whole source volume) is difficult. Another possibility is to only lower the partial pressure of tritium.
A low magnetic source field leads to magnetic reflection of most electrons back to the rear section. Possible scenarios are discussed in section 2.2.
Some of the other main systematic effects are listed below.

- Inelastic scattering with gas molecules in the WGTS
- Magnetic traps in different parts of the setup (e.g. source and spectrometer) [Kna17]
- Non-adiabatic momentum transformation in the spectrometer for electrons with high surplus energies [Hub15]
- Backscattering, Pile-up and charge sharing at the detector [Dol16]

Another important systematic effect are backscattering processes of electrons on the Rear Wall. Its impact and possible countermeasures are the subject of this thesis.

2. The rear wall as a systematic effect for a keV-scale sterile neutrino search

The rear wall at the upstream end of the WGTS is a gold-plated stainless steel plate. It is located in the rear wall chamber that can be seen in fig 2.1. A small hole in its middle allows electrons produced by the e-gun to enter the beam tube.
Before and during normal KATRIN mode the rear wall fulfills many tasks [KAT05]. These are:

- Emission of photo-electrons during first light measurement through illumination with UV-light. These are used to measure the capability of the setup to guide electrons from the source to the detector.
- Through scattering with gas molecules β-electrons create many secondary electrons and ions. To ensure charge homogeneity in the WGTS photo-electrons are used to neutralize the ions. These photo-electrons are generated by illuminating the rear wall with UV-light.
- Definition of the overall source potential.
- Monitoring of the source strength by measuring the intensity of γ-rays from the rear wall. These photons are bremsstrahlung generated by β-electrons on the rear wall.

2.1. Staged approach for a keV-scale sterile neutrino search

The search for keV-scale sterile neutrinos with KATRIN is divided into two separate measurements. The phase-0 data-taking will prospectively take place before KATRIN neutrino mass data taking starts. It will be a low-statistic measurement used to get deeper understanding of how the KATRIN setup can be used to detect a keV-scale sterile neutrino. For phase-0 no major changes can be made on the KATRIN hardware setup. However, the magnetic and electric fields as well as the amount of tritium in the source can be modified. To measure the entire β-decay spectrum, the retarding potential of the main spectrometer has to be lowered to small values or even zero. The high luminosity source of KATRIN has a decay rate of 10^{11} decays per second [KAT05], which would lead to a high rate of $1.5 \cdot 10^{10}$ cps at the detector, in non-retarding mode [B$^+$16]. The detector can only handle rates of the order of 10^5 cps [B$^+$16]. To not over-strain the detector at least a reduction of $f_{red} = 10^5$ is needed.
Phase-1 will take place after the neutrino mass measurement. For this high-statistic investigation updates on the setup are necessary. Most important will be a new detector that can handle high count-rates at a still very good energy resolution. A prototype of this detector, the TRISTAN detector, is currently under investigation and a second prototype will be built soon [Dol16].
The investigation on backscattering on the rear wall covered in this thesis focuses on the phase-0 measurement. These studies will be extended to design an optimal rear wall for phase-1.

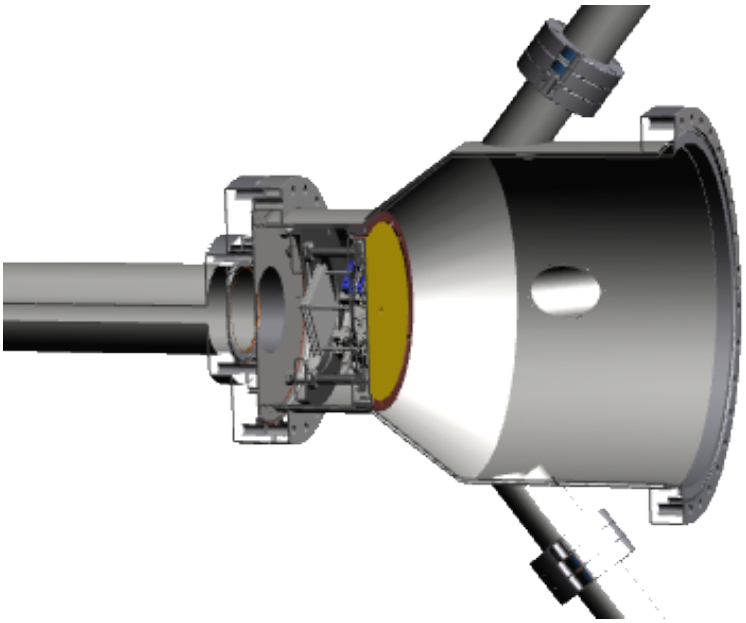


Figure 2.1.: Setup of the rear wall chamber at the upstream end of the WGTS. The gold rear wall can be seen on the left side of the chamber.

2.2. The KATRIN setup for the phase-0 measurement

To achieve the aimed rate reduction, so that the KATRIN focal plane detector can be used, two different scenarios are discussed [Hub16]. For both the amount of tritium in the source[1] needs to be reduced.

1. Scenario 1: Reduction of the acceptance angle.
   According to equation 1.13, a small source field leads to an increased magnetic reflection of β-decay electrons (latest at the pinch magnet). With a source magnetic field of 450 G, the reduction[2] of the amount of electrons that are able to reach the detector without being reflected will be $f_{\Theta_{\max}} = 5.32 \cdot 10^2$. Additionally a source reduction of $f_\rho = 187$ would be needed [Hub16]. All electrons that were magnetically reflected on their way to the detector fly towards the rear wall. The $8.02 \cdot 10^7$ electrons per second that are generated in the WGTS, result in $1.51 \cdot 10^5$ cps at the detector and $8.01 \cdot 10^7$ cps at the rear wall. Therefore any effect caused by electrons at the rear wall is amplified by a factor of $5.31 \cdot 10^2$. The calculations in this thesis are based on this scenario, its overall magnetic setting[3] is shown in figure 2.2.
2. Scenario 2: Reduction of the tritium activity.
   Here the highest possible source field of 0.5 T is used. An even higher magnetic field in the source would cause a too broad flux tube in the pre-spectrometer, and the adiabatic transport through the main-spectrometer is endangered [B$^+$16]. With the given magnetic field the source needs to be reduced by a factor of $f_\rho = 2.13 \cdot 10^3$. Now rear wall effects are only amplified by a factor of 46.0.
3. Scenario 3: Backup.
   If it should not be possible to lower the source strength by more than a factor of

[1] Less tritium in the source can either be achieved by lowering the gas density or by reducing the fraction of tritium in the gas.

[2] A certain reduction means that dividing the initial count-rate by the reduction factor gives the new count rate.

[3] This setting is the one agreed on right now, it might however still change. Here all Simulations and considerations were made for the setting on hand.

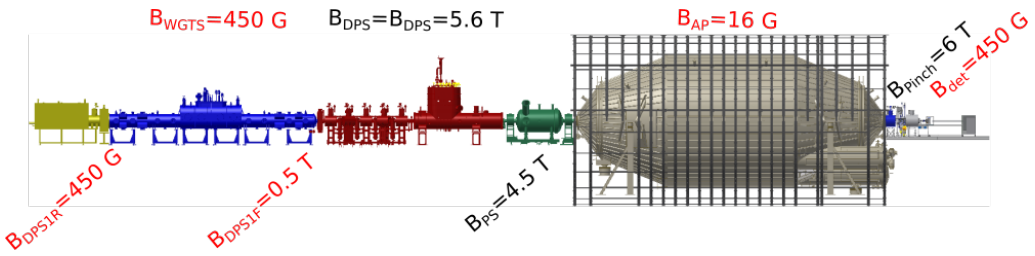


Figure 2.2.: Magnetic fields in the KATRIN setup run in phase-0 mode. The shown fields correspond to rate-reduction scenario 1. In red all the magnetic fields that differ from the normal KATRIN mode. Values from [Hub16].

100 also a third scenario needs to be considered. Again the lowest possible field in the WGTS will be used. To ensure low enough count rates at the detector the spectrometer needs to be operated at retarding potentials bigger than 5 keV. Because of the same magnetic field setting, effects at the rear wall are amplified by the same factor as for scenario 1.

From now on 'phase-0 mode' will refer to the setting shown in figure 2.2. In normal KATRIN mode the magnetic setting and diameter of the source (including safety margin to walls) lead to a sensitive magnetic flux of 191 T cm^2 [KAT05]. In contrast, in the phase-0 mode, a source field of $B = 450\,\mathrm{G}$ is applied, and a larger safety margin needs to be used. Electrons with an energy perpendicular to the magnetic field of $E_\perp = 20\,\mathrm{keV}$ have a cyclotron (Larmor) radius of roughly

$$r_\mathrm{L} = \frac{\sqrt{2 m_e E_\perp}}{eB} \approx 1.0\,\mathrm{cm}. \tag{2.1}$$

m_e and e are mass and charge of the electron. A reasonable safety margin therefore is to keep the sensitive flux tube at least 1 cm away from the beam tube walls. With a geometrical beam tube radius of 4.5 cm [KAT05] in the WGTS the flux tube would only be allowed a radius of $r_\mathrm{WGTS} = 3.5\,\mathrm{cm}$ resulting in an overall flux of

$$\Phi = B_\mathrm{WGTS} \cdot A_\mathrm{WGTS} = B_\mathrm{WGTS} \cdot \pi r_\mathrm{WGTS}^2 = 1.73\,\mathrm{T\,cm}^2. \tag{2.2}$$

2.3. Backscattered and Auger electrons from the rear wall

All electrons heading towards the rear section eventually arrive in the rear wall chamber and hit the rear wall or the rear wall chamber walls, depending on where the magnetic field lines guide them. Through (multiple) scattering processes in the material some electrons are not absorbed but exit the rear wall again (see figure 2.3). During this backscatter process they experience a certain energy and angular change. The backscatter probability as well as the properties of the electron after scattering depend on their initial energy, the impact angle and the target material.

Also an incident electron can create secondary electrons in the target material. It could for example ionize a gold atom of the rear wall plate, by ejecting an electron from a lower shell. The de-excitation of the atomic shell can happen through the emission of an Auger electron:

An electron from a higher shell falls down into the vacancy left by the ejected electron. The released energy can be transferred to another electron in the atom which is then ejected. This Auger electron possesses a specific energy. It depends on the released transition energy and the energy needed to eject the Auger electron (see figure 2.4).

For a certain material characteristic Auger lines can be seen in the energy spectrum of secondary electrons. For a gold rear wall the production and imprint of Auger electrons is

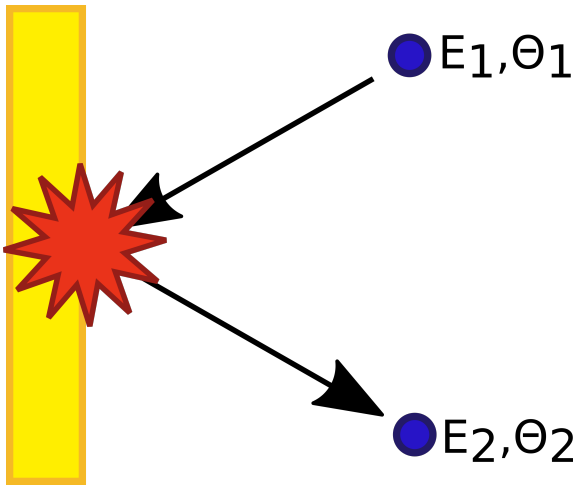


Figure 2.3.: When an electron hits a target material it is not necessarily absorbed but can get backscattered. Thereby its energy and angle mostly changes. The probability to backscatter as well as the change of properties depend on the target material, initial energy and angle of the electron.

discussed in section B.2.

In the phase-0 mode many electrons hit the rear wall with different energies and angles. Hence many backscattered and secondary electrons are created and need to be considered. For a look on the backscatter spectrum of mono-energetic electrons see figures 2.7 and 2.6. The most important question is, how many of these electrons can reach the detector? As they do not carry β-decay information (any more) their signals at the detector are an unwanted systematic background.

The simulations (described in detail in sections 3.2.1 and 3.2.2) show, that with no countermeasures the spectral distortion, caused by backscattered and secondary electrons, would be of the order of 90% (see figure 3.12) in scenario 1 and 80% in scenario 2. The effect is enhanced in scenario 1 since in this case, the column density of tritium in the source is higher, and therefore the fraction of electrons hitting the rear wall is enhanced as compared to the detector.

2.4. Countermeasures

To reach the aimed sensitivity of 10^{-3} in the phase-0 sterile neutrino search all systematic effects need to be suppressed as much as possible [Mer16]. It is crucial to allow as little as possible backscatter[4] processes to occur and to hinder backscattered electrons from reaching the detector. There are three different parameters one can control during phase-0 to influence the systematic effect of backscattering on the rear wall:

1. The magnetic field at the rear wall can be varied by changing the currents in the rear section magnets.
2. Instead of using the currently installed gold rear wall a beryllium rear wall could be installed.
3. By lowering the tritium source activity, the acceptance angle (source magnetic field, see section 1.2.1 can be increased and hence less electrons hit the rear wall (see section 2.2).

In the following, the influence of the three different parameters on the backscattering of electrons on the rear wall will be discussed in more detail.

[4]When talking of backscattering always also the production of secondary electrons is meant.

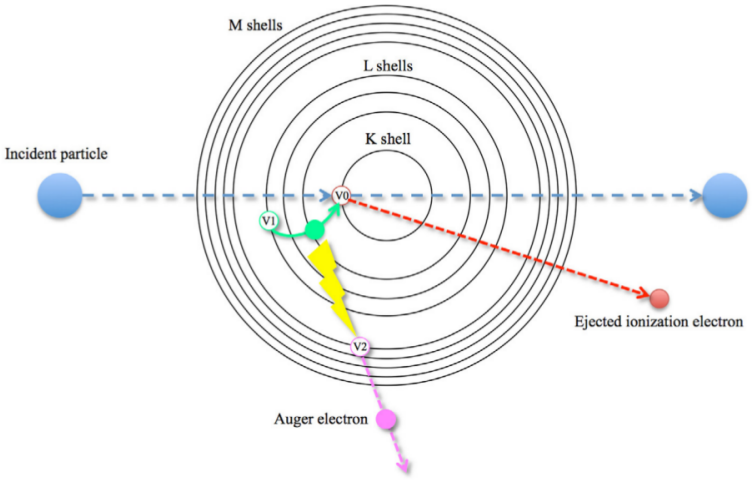


Figure 2.4.: An incident particle, eg. an electron, can ionize a target atom. The vacancy left by the ejected electron is filled with an electron from a higher shell and a certain amount of energy (depending on the different shell potentials) is released. This energy can be transfered to another electron (Auger electron) in the atom which is then able to escape. For different materials Auger electrons have specific energies, depending on the released energy when filling the inner vacancy and the ionization energy needed to eject the Auger electron. The filling of vacancies with outer shell electrons (vacancy from initial ionization, from the electron that filled that vacancy and the Auger-vacancy) up to complete relaxation of the shell is called Auger-cascade. Figure from [I+16].

Magnetic field

The magnetic field at the rear wall is a superposition of the stray field from the DPS and WGTS magnets as well as the rear section magnets (see figure 3.2). Only the magnetic fields in the rear section will be changed, causing different fields at the point of impact of the electrons at the rear wall.
Because of the conservation of the overall flux of $1.73\,\mathrm{T\,cm^2}$ (compare equation 2.2) the magnetic field at a certain point in the setup defines the radius of the sensitive flux tube at that point. For example a very low field at the rear wall would cause a broad flux tube. Since the gold rear wall radius is only 7.5 cm for fields lower than 98 G not the whole flux tube fits on it. In that case electrons guided along the outer field lines of the flux tube do not hit the gold of the rear wall but the stainless steel that surrounds it. A short discussion on the possible influences of stainless steel backscattering can be found in A.2.
In section 1.2.1 magnetic reflection was introduced and the fact, that an electron starting with an angle lower than the acceptance angle Θ_{max} (relative to the magnetic field, see equation 1.13) and heading towards higher magnetic fields is not reflected.
In the WGTS electrons are generated with an isotropic angle distribution. For the magnetic setting shown in figure 2.2 only electrons with initial angles below 5° manage to get past the 6 T at the pinch magnet. The fraction of electrons that are able to reach the detector compared to those that do not, corresponds to the transmission probability P_{trans}. It depends on the field B_{ini} the electrons is created in. For an isotropic distribution (for electrons from the WGTS) it is given by

$$P_{\mathrm{trans}}^{\mathrm{WGTS}} = \frac{1}{2}\cdot(1-\cos\Theta_{\mathrm{max}}) = \frac{1}{2}\cdot\left(1-\sqrt{1-\frac{B_{\mathrm{ini}}^{\mathrm{WGTS}}}{B_{\mathrm{max}}}}\right). \tag{2.3}$$

The 1/2 takes into account that only electrons initially heading towards the detector (drawn through cone in figure 2.5) are considered.
Backscattered electrons also have a transmission probability from the rear wall to the

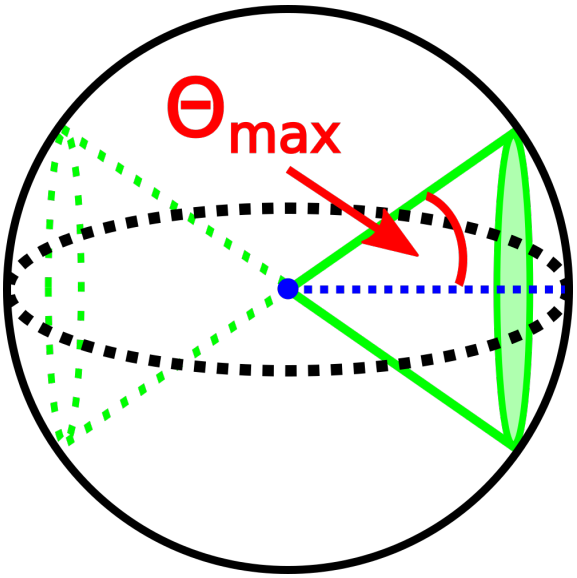


Figure 2.5.: In the WGTS electrons are generated with isotropic angle distribution (from 0° to 180° relative to the magnetic field). However only those with an angle below the acceptance angle Θ_{max} manage to reach the detector (green drawn through cone). This fraction of the total solid angle corresponds to the transmission probability P_{trans} for electrons from the WGTS to the detector.

detector. Since they only have angles between 0° and 90° (only half of the total solid angle) the transmission probability for backscattered electrons is

$$P_{\text{trans}}^{\text{RW}} = 1 - \sqrt{1 - \frac{B_{\text{ini}}^{\text{RW}}}{B_{\text{max}}}}. \tag{2.4}$$

Here $B_{\text{ini}}^{\text{RW}}$ is the magnetic field incident electrons experience when hitting the rear wall. Note that an isotropic angle distribution (from 0° to 90°) of the backscattered electrons is assumed.

The magnetic field does not only influence the point of impact and the transmission probability of backscattered electrons. Also the maximum impact angle of electrons on the surface (relative to perpendicular) is determined by the change of magnetic field they experience when heading from the WGTS to the rear wall. As described in section 1.2.1 the momentum of an electron traveling towards lower magnetic fields gets more and more shallow. Therefore, no electrons hit the surface with angles higher than the maximum impact angle $\Theta_{\text{imp}}^{\text{max}}$, that is defined through the field in the WGTS and at the rear wall (compare equation 1.13). As already mentioned different impact angles have a significant influence on backscattering. The more shallow an electron hits the surface the higher is the probability for backscattering as can be seen in figure 2.6.

Rear wall material

Different materials show very different backscatter behaviors. The three materials of interest are compared in figure 2.7. Currently a gold rear wall is installed in the KATRIN setup. Figure 2.7 however shows, that gold possesses a very high backscatter probability (the results from GEANT4 shown in 2.7 state, that 50% of 20 keV mono-energetic electrons get backscattered). As already discussed in the previous paragraph electrons might not only hit the rear wall material but also the stainless steel around it. Stainless steel shows a lower backscattering probability than gold. With only 2% beryllium shows the lowest backscatter probability of the materials in figure 2.7.

When electrons penetrate a material they either scatter with the atomic nuclei or the

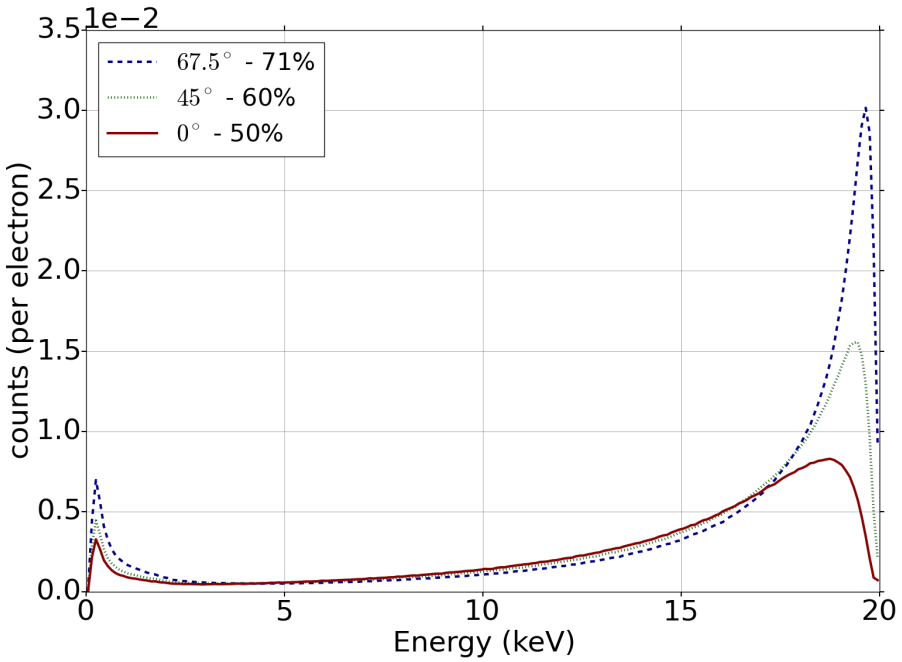


Figure 2.6.: Energy distribution of backscattered electrons from a gold surface. All electrons had an initial energy of 20 keV and headed onto the target with different angles to the perpendicular. The percentage in the legend states how many incident electrons get backscattered. The more shallow electrons hit the surface, the more get backscattered.

electrons in the shells. Electron-electron scattering mostly only causes small angular changes [KEHM82]. For backscattering however high angular changes are necessary and hence scattering with nuclei. The higher the atomic number the higher the cross section for electron-nucleus scattering. As beryllium has a very low atomic number of 4 the probability for backscattering is small.

Therefore, plans are made to use a beryllium rear wall instead of gold [Rin16]. Such a beryllium wall would be installed within the rear wall chamber, located further to the WTGS than the gold rear wall (compare figure 2.8).

Source strength

As a result of the aimed rate reduction at the detector, almost 10^3 times more electrons reach the rear wall compared to the detector. In scenario 2 a much higher source field is applied and hence a higher source reduction demanded. Considering rear wall backscattering this is a favored setting, because less electrons are generated and hence less electrons backscatter on the rear wall.

However, it is still not certain how much the source strength can be lowered. The source stability may not be guaranteed for low column densities. Nevertheless a short investigation on this scenario will be discussed. Note, that in this scenario an other overall flux needs to be considered:

$$\Phi = B_{\mathrm{WGTS}} \cdot A_{\mathrm{WGTS}} = B_{\mathrm{WGTS}} \cdot \pi r^2_{\mathrm{WGTS}} = 19.2\,\mathrm{T\,cm^2}. \tag{2.5}$$

Therefore a higher field at the rear wall is needed to focus the whole sensitive flux tube on the rear wall.

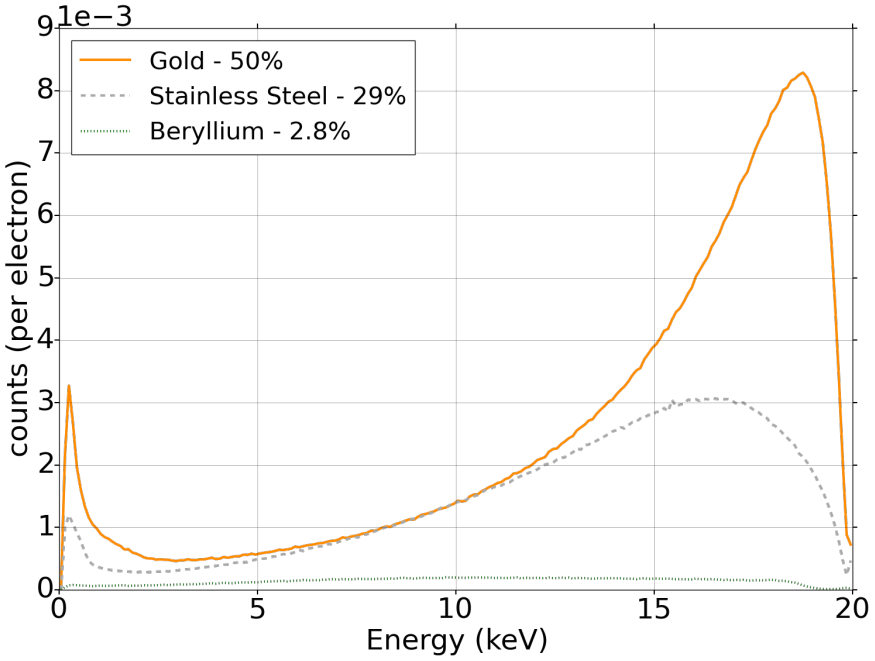


Figure 2.7.: Energy distribution of backscattered electrons for different target materials. All electrons had an initial energy of 20 keV and headed perpendicular on the target. Different materials show very different backscatter behaviors. The percentage in the legend states how many incident electrons get backscattered (backscatter probability). Obviously on gold the most electrons get backscattered and on beryllium the least. Also the energy losses during backscattering show different shapes (shape of the tail below 20 keV)

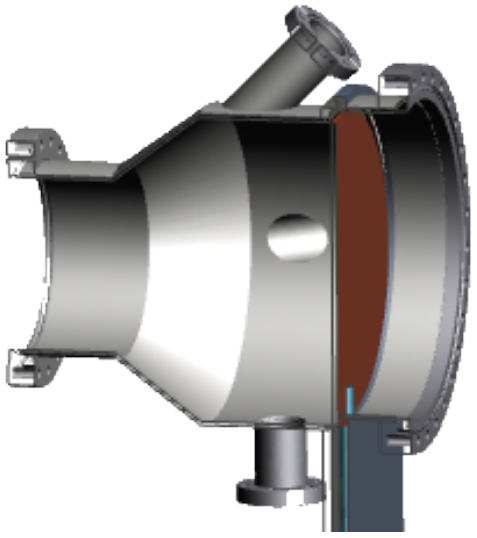


Figure 2.8.: A beryllium rear wall would be installed in the rear wall chamber. It is then located 17 cm apart from the gold rear wall plate, further towards the WGTS. Figure from [Rin16].

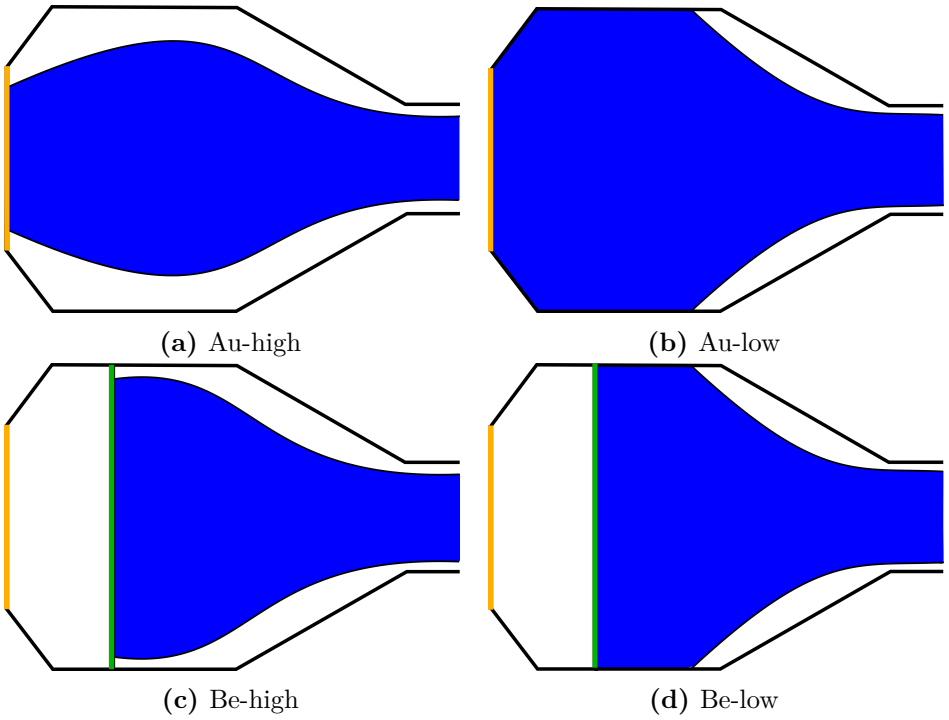
3. Results of the Thesis

3.1. Discussed scenarios

Based on the different possible countermeasures discussed in section 2.4 different scenarios are investigated:

- Scenario 1 (with a tritium reduction of $f_\rho = 187$, see section 2.2)
  - Gold rear wall + high magnetic field: Au-high
    The 'default' setting is when all field lines of the sensitive flux tube hit the gold rear wall. This case will be referred to as 'Au-high' case because here the field at the rear wall is high enough to focus the whole flux tube on the wall.
  - Gold rear wall + reduced magnetic field: Au-low
    Starting from the default case the easiest way to decrease the effect is to lower the field at the rear wall as much as possible, referred to as 'Au-low' case. Then the impact of the stainless steel walls for the outer detector rings needs to be considered. The lowest and highest impact of stainless steel (SS) backscattering will be investigated (SS-low and SS-high).
  - Beryllium rear wall + high magnetic field: Be-high
    If the effect is still not minimized enough by the two previous cases a beryllium rear wall could be installed as described in section 2.4. Again a certain field is needed to focus the flux tube on the rear wall plate.
  - Beryllium rear wall + low magnetic field: Be-low
    Again the lowest possible field is reached by turning off all rear section magnets.
- Scenario 2 (with a tritium reduction of $f_\rho = 2.13 \cdot 10^3$):
  - Gold rear wall + high magnetic field:
    Again proceeding from a flux tube focused on the gold rear wall a short investigation will be discussed on scenario 2 from section 2.2.

The cases for scenario 1 are shown in figure 3.1.
Section 2.4 showed that the magnetic field at the point of impact of the electrons influences many parameters such as the transmission probability for backscattered electrons. Hence the first step is to determine this magnetic field for the different scenarios. This was achieved with KASPER, as described in the following section.
Using this information the backscatter spectrum (including the production of secondaries) was simulated with GEANT4. Eventually the backscattered electrons are propagated to the detector (transmission probability) and compared to the electron spectrum coming from the WGTS.
The different steps are discussed in detail for the 'Au-low' scenario including all inputs



(a) Au-high **(b)** Au-low

(c) Be-high **(d)** Be-low

Figure 3.1.: Rear wall chamber, with gold (orange) or beryllium (green) rear wall, and sensitive flux tube (in blue). Shown are the different cases discussed for the scenario 1 (see figure 2.2). In figures 3.1a and 3.1b the gold rear wall is illuminated with either the total flux tube (Au-high, 3.1a) or only parts of it (Au-low, 3.1b). Also for the beryllium rear wall (3.1c and 3.1d) the total flux tube can be focused on the wall or the lowest possible field applied.

for the simulations and approximations that were made. All other scenarios were treated equally. Their results can be seen in section 3.3.

3.2. Simulation Method

3.2.1. KASPER simulations

The simulation package KASPER was specifically developed for the KATRIN experiment. It is capable of calculating electric and magnetic fields in a pre-defined geometry. Additionally different particles can be generated and tracked in the fields. The geometry of the KATRIN experiment is implemented and can be easily used for simulations in different parts of the setup. KASPER uses XML configuration files in which for example the currents in the magnetic coils can be defined.
For the investigation of rear wall scattering electrons were tracked within the magnetic fields of the different settings. Scattering with gas atoms in the beam tube as well as cyclotron motion around the field lines (so called magnetic tracking) were not taken into account. All electrons fly along the magnetic field lines.
In all KASPER simulations presented in this thesis the geometry from the rear section up to the CPS was included and hence all fields originating from solenoids in this area of the experiment. Figure 3.2 shows the geometry as it is included in the simulations and the names of the different solenoids as they appear in the configuration file. Note that the different accesses to the rear wall chamber shown in figures 2.1 and 2.8 are not included in the simulation geometry in figure 3.2.
All DPS- and CPS-coils are run with nominal (KATRIN-mode) currents that generate magnetic fields of 5.6 T (compare figure 2.2). DPS1R and WGTS magnets induce a field of 450 G. To ensure adiabatic transport of electrons from the source to the transport section

the DPS1F magnets generate a field of 0.5 T. All rear section magnets are turned off excluding the RSCM-main magnets that are used to generate a certain field at the rear wall.
Electrons are generated in the middle of the WGTS with an energy of 2 keV. Their momentum is parallel to the magnetic field and pointing towards the rear section. For each setting 350 electrons with different initial radii in the beam tube from 0 cm to 3.5 cm were generated and tracked until they hit the walls of the rear wall chamber or the rear wall plate.
All output parameters are written into a root file. The track output contains information about generation and termination of the particle (initial and final values). It includes information about position and momentum of the particle as well as the electric and magnetic fields, given in three spacial coordinates.
The point of impact depends only on the initial radius r_{ini} since the setup is radially symmetric and the size of the flux tube at the rear wall is defined by the magnetic field. The final magnetic field at the point of termination of the electrons (on the walls) is given in three coordinates $B_{\mathrm{fin,x}}$, $B_{\mathrm{fin,y}}$ and $B_{\mathrm{fin,z}}$.

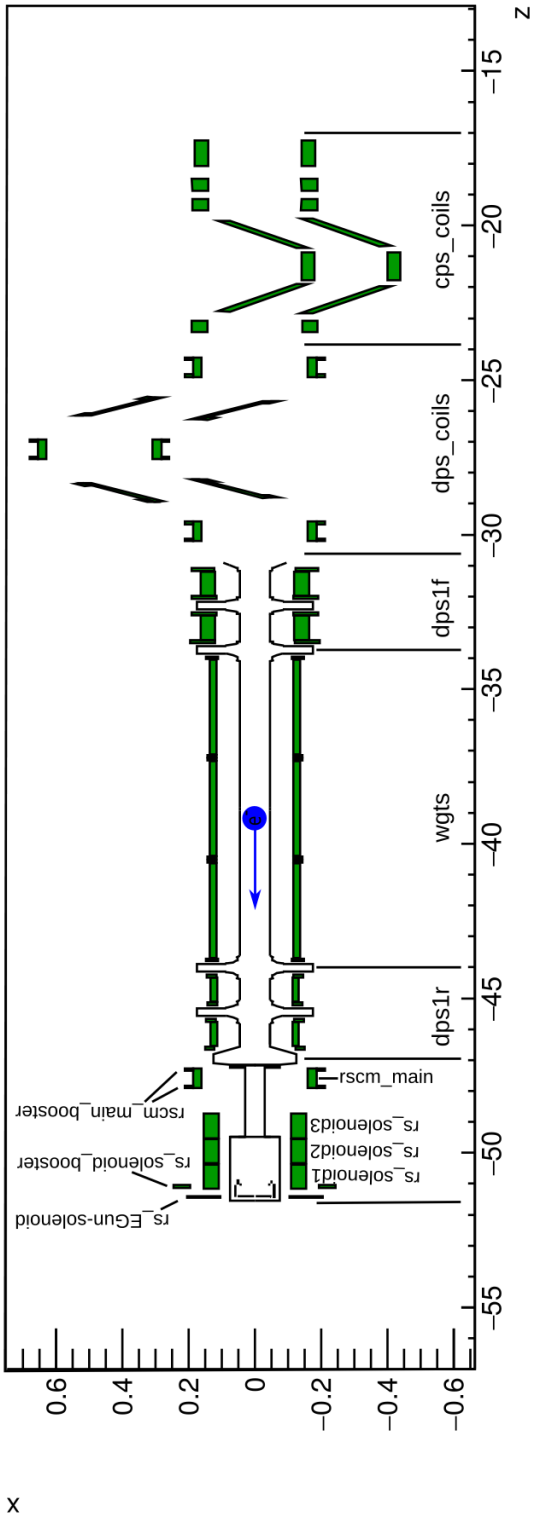


Figure 3.2.: In the performed KASPER simulations the KATRIN setup from rear section to CPS was considered. All CPS magnets were run with their nominal (KATRIN-mode) currents, the same applies for the DPS-coils. The WGTS and DPS1R magnets were set to cause a field of 450 G in the beam tube. To ensure adiabatic transport from source to transport section the field at the DPS1F magnet equals 0.5 T. To vary the field at the rear wall only the RSCM-main magnets are used, all other rear section magnets are turned off in the simulation. Electrons are generated in the middle of the WGTS and head parallel to the magnetic field towards the rear section.

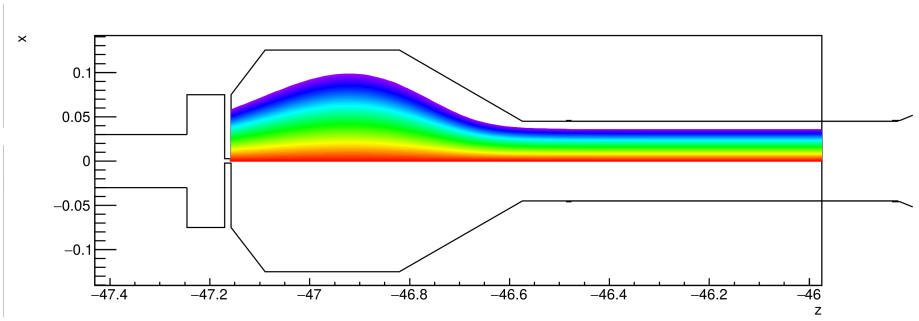


Figure 3.3.: Au-high: Rear wall chamber with electron trajectories coming from the WGTS. The trajectories were simulated with KASPER. The color represents their initial radius. The rainbow colored area corresponds to the total sensitive flux tube. All electrons hit the rear wall.

Processing of simulation results

The total magnetic field at the point of impact of the electron on the rear wall plate B_{imp} is given by

$$B_{\text{imp}} = \sqrt{B_{\text{fin,x}}^2 + B_{\text{fin,y}}^2 + B_{\text{fin,z}}^2}. \tag{3.1}$$

Here $B_{\text{fin,i}}$ are the magnetic fields in all three spacial directions at the point where electrons hit the wall, given as simulation output from KASPER. The final magnetic field an electron experiences depends on its radial position within the flux tube. Figure 3.4 therefore shows the dependence of B_{imp} on the relative flux tube radius r_{rel} given by

$$r_{\text{rel}} = \frac{r_{\text{ini}}}{3.5\,\text{cm}}.$$

With r_{ini} being the initial radius of the electron. The radius of the sensitive flux tube within the WGTS is 3.5 cm. The radial position at any other point in the geometrical setup can be calculated by multiplying the relative radius with the radius of the flux tube at that point, and hence depends on the magnetic field at that point.
For scenario Au-high the electron trajectories calculated by KASPER are shown in figure 3.3. Because of the cyclotron motion of the electrons a safety margin to the edge of the wall needs to be kept. Its calculation is described in the appendix, section A.1. Hence in figure 3.3 the sensitive flux tube (rainbow colored area) does not illuminate the whole rear wall.
For figure 3.4 the magnetic field at the point of impact for the Au-high scenario was calculated, it shows that the magnetic field at the rear wall varies from about 165.5 G at the outer flux tube regions up to almost 170 G in the middle. The jump for very small radii is caused by the e-gun hole in the rear wall. Here the electrons do not hit a wall but are able to propagate a little further into the rear section. As it is not clear what happens to those electrons they will be excluded from the further investigation.
To simplify further investigations the radial variation of the magnetic field will be approximated with a constant mean magnetic field $\bar{B}_{\text{RW}}$ for the whole rear wall. Excluding the red shaded area in figure 3.4 it holds

$$\bar{B}_{\text{RW}} \approx 168.3\,\text{G}.$$

This field causes a maximum impact angle of electrons hitting the rear wall of (compare equation 1.13)

$$\Theta_{\text{imp}}^{\text{max}} = \arcsin\sqrt{\frac{\bar{B}_{\text{RW}}}{B_{\text{WGTS}}}} \approx 37.7°$$

and a transmission probability for backscattered electrons of (equation 2.4)

$$P_{\text{trans}}^{\text{RW}} = 1 - \sqrt{1 - \frac{\bar{B}_{\text{RW}}}{B_{\text{max}}}} \approx 1.4 \cdot 10^{-3}.$$

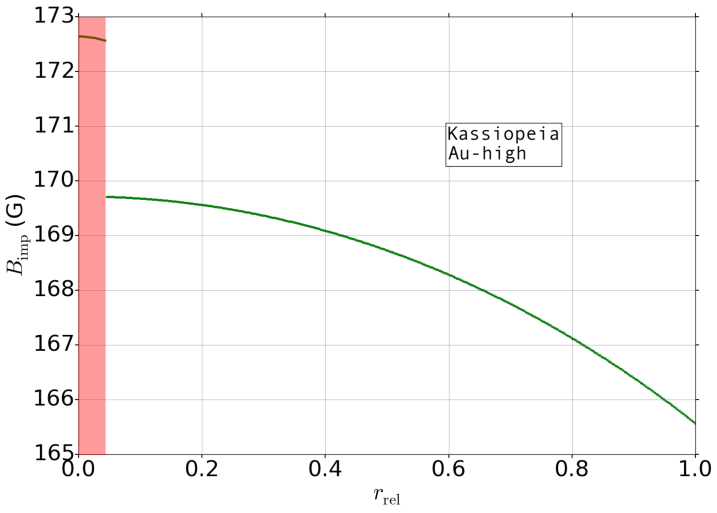


Figure 3.4.: Au-high: Total magnetic field at the point of impact of electrons on the rear wall B_{imp} versus the relative flux tube radius of the electron r_{rel}. The magnetic field at the rear wall is not constant. The jump at low radii is cause by the e-gun hole in the rear wall. All electrons that enter it are excluded from further investigation.

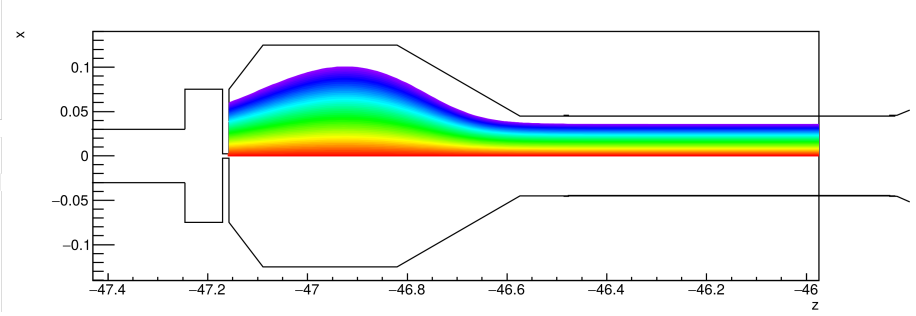


Figure 3.5.: Scenario2: Rear wall chamber with electron trajectories coming from the WGTS. The color represents their initial radius. The rainbow colored area corresponds to the total sensitive flux tube.

Scenario 2

The motivation for using a higher source field and much less tritium in the source is to reduce the count-rate at the rear wall. For a high tritium reduction less electrons need to be magnetically reflected to the rear wall to reduce the count-rate at the detector. With a source field of 0.5 T (DPS1R, WGTS, DPS1F) only 46 times more electrons reach the rear wall compared to the detector. Because of the higher overall flux in this setting of $\Phi = 19.2\,\mathrm{T\,cm^2}$ a field of at least 1086 G is needed to focus the flux tube on the gold rear wall. Including a safety margin for cyclotron motion the KASPER simulation gives a mean magnetic field on the rear wall of $\bar{B}_{\mathrm{RW}} = 1760.58\,\mathrm{G}$ (compare table 3.1). Figure 3.6 shows the variation of the magnetic field on the rear wall. The electron trajectories for scenario 2 can be seen in figure 3.5.

For the other scenarios the same approach was applied. Any differences and the results from the KASPER simulations are described in the appendix A.2. All values gained from KASPER simulations for each scenario are summarized in table 3.1.

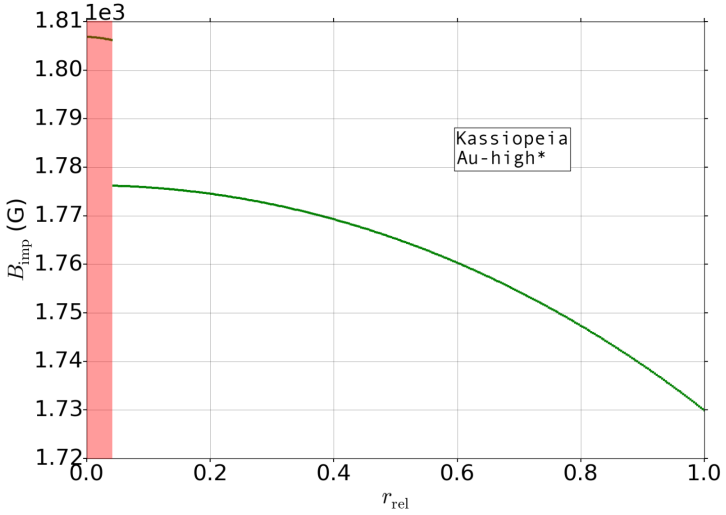


Figure 3.6.: Scenario2: Total magnetic field at the point of impact of an electron on the rear wall and surrounding walls B_{imp} versus the relative flux tube radius of the electron r_{rel}.

Table 3.1.: Different discussed scenarios and mean field at the point of impact as a result from the KASPER simulations. The maximum impact angle $\Theta_{\mathrm{imp}}^{\mathrm{max}}$ is used as input for the GEANT4 simulations. With the transmission probability P_{trans} the backscatter spectrum (output from GEANT4 simulation) is propagated to the detector.

	Scenario 1						Scenario 2
	Au-high	Au-low	Be-high	Be-low	SS-low	SS-high	
B_{imp} (G)	168.3	8.37	44.54	16.51	8.26	33.86	1760.58
$\Theta_{\mathrm{imp}}^{\mathrm{max}}$ (°)	37.7	7.8	18.3	11.0	7.8	15.9	36.4
P_{trans}	1.40E-03	6.98E-05	3.71E-04	1.38E-04	6.88E-05	2.82E-04	1.48E-02

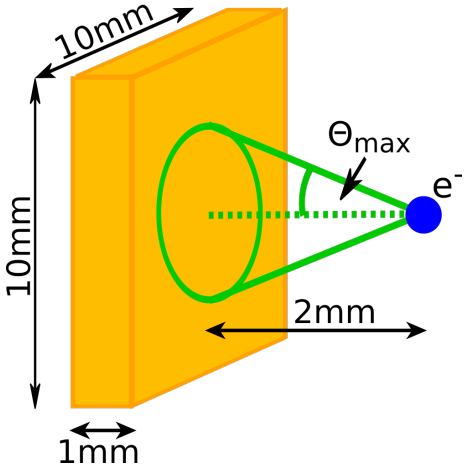


Figure 3.7.: In the GEANT4 simulations electrons are generated and send on the target. They head at it with different angles (isotropically distributed up to a maximum impact angle).

3.2.2. GEANT4 simulations

The GEANT4 monte carlo simulation toolkit can simulate the propagation of particles through matter [Gea]. When propagating the particles different interactions, like ionization and scattering, can be included. It is mostly used for simulations of high energy particles but is also an interesting tool for low energy ranges. Electrons from tritium β-decay with energies up to 18.6 keV fall under this regime. Since the upgrade to version 10.1 in 2014 a more precise de-excitation of the electron shells including the full Auger-cascade as described in figure 2.4 was implemented [I+16].
The following simulations were produced with the release GEANT4.10.2 from the 4th of December 2015. A slightly altered version of the TestEm5[1] example was used, modified to use the general particle source (GPS) and stainless steel as target material[2]
The TestEm5 executable is configured via a macro file, where material and geometry of the target, type of particle, its energy and direction and the included physics packages and processes can be defined. For the simulation of backscattering the Livermore physics package was used and Auger electron production and cascade included.

Settings for the GEANT4 simulation

The GEANT4 simulations all used the same geometry. Electrons are generated at a distance of 2 mm apart from a cuboid target with an edge length of 10 mm and a thickness of 1 mm. This setup can be seen in figure 3.7.
In all simulations (except for Scenario 2) 10^9 electrons are generated and hit the target material. For the low statistic investigation on scenario 2 only 10^7 electrons were simulated, to reduce the needed simulation time. The impact angle varies isotropically from 0° to the maximum impact angle $\Theta_{\text{imp}}^{\text{max}}$ (listed in table 3.1). The energy distribution of the generated electrons is defined via a histogram with 200 bins from 0 keV to 20 keV following the tritium β-decay energy spectrum. The input energy distribution is shown in figure 3.8.
As simulation output, different histograms can be chosen. For the present investigations

[1] TestEm5 is an already built example for low energy electromagnetic simulations. Many materials and commands are already defined.
[2] Stainless steel was built by defining the fraction masses of the different components of the stainless steel type used in the rear wall chamber. The rear wall chamber vessel is made of stainless steel type 1.4429 ESU (316LN). It therefore consists of roughly 62% iron, 18% chromonium, 14% nickel, less than 3% molybdenum and 2% manganese as well as small amounts of carbon, silicon, sulfur and phosphor.

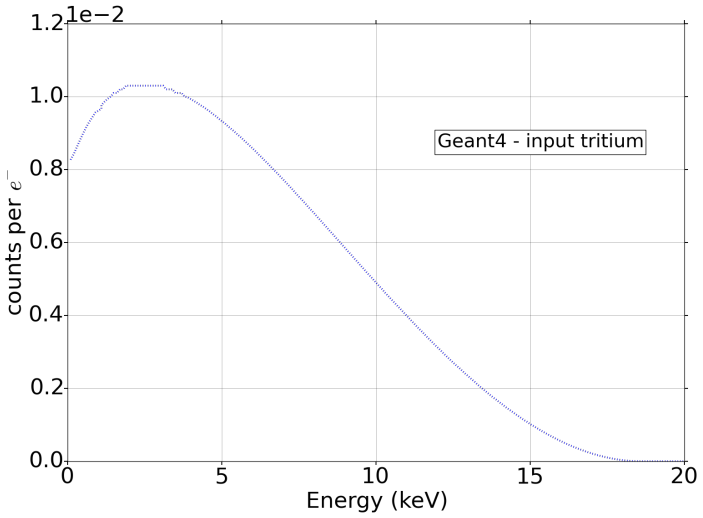


Figure 3.8.: The energy of electrons generated from GEANT4 is distributed according to the above β-decay spectrum. It consists of 200 bin from 0 keV to 20 keV.

the energies of all reflected charged particles are of interest. The output is a histogram that counts what energies electrons have, that exit the target on the same side the initial electrons entered it. Since the input tritium-spectrum consists of 0.1 keV bins the output is binned correspondingly, into 200 bins from 0 keV to 20 keV.
The output histogram with the energies of reflected particles will, from now on, be refereed to as 'backscatter spectrum at the rear wall'. For each scenario a simulation with and without activated Auger process was performed. By comparing the two results one can estimate how many Auger electrons were produced[3]. The used approximation is the difference of the overall number of reflected particles with and without activated Auger process:

$$N_{\text{Auger}} \approx N_{\text{reflected,with}} - N_{\text{reflected,without}}. \tag{3.2}$$

For backscattering on a gold target and an isotropic angle distribution up to 37.7° (Au-high) a tritium spectrum transforms into the backscatter spectrum shown in figure 3.9. The figure also shows the difference of a simulation with and without Auger processes turned on.
Excluding scenario 2, the same simulations were done for the other scenarios listed in table 3.1, only varying the input parameters target material and maximum impact angle according to the values given in the table.
For better comparison, all spectra are normalized to the number of initial electrons N_{RW}. For scenario 2 only a short low-statistic investigation, with 10^7 electrons, was simulated with GEANT4. Apart from that the simulation settings remained the same. All results from the GEANT4 simulations are listed in table 3.2. The corresponding spectra with backscattering and ratio plots can be seen in the appendix B.1.

3.3. Analysis of simulation results

With the KASPER simulations the magnetic fields on the rear wall were gained (compare section 3.2.1 and table 3.1). The following enumeration explains in what steps these results were processed and how the overall backscatter spectrum at the detector was calculated.

[3]The number of produced Auger electrons can only be an approximation, because these secondary electrons can also cause ionization and other secondary effects. It is not possible to flag electrons, that were generated as Auger electrons. Hence one does not know how many of the additional electrons that are produced with activated Auger processes are in fact original Auger electrons.

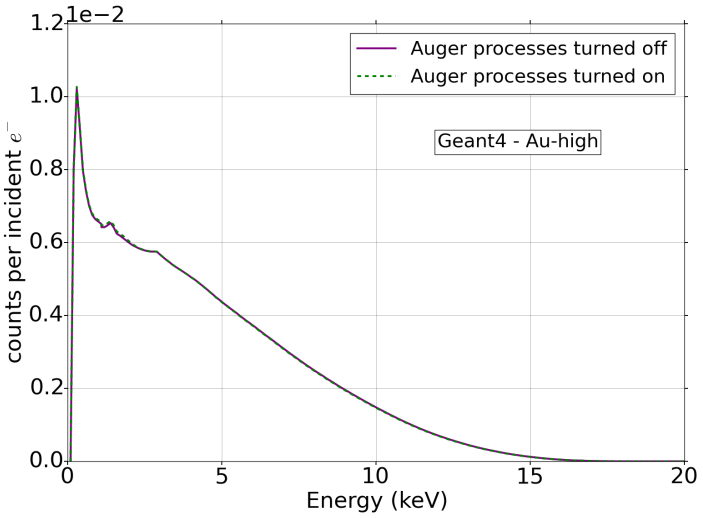


Figure 3.9.: Au-high: Backscatter spectrum as it would be measured at the rear wall, normalized to one incident electron. The course of the backscattered spectrum differs a lot from the initial tritium spectrum shown in figure 3.8. For the purple (drawn through) spectrum all Auger processes were turned off. A small difference can be seen at energies of about 2 keV.

The task of GEANT4 is the simulation of the backscatter spectrum in part 4. The different steps are illustrated in figure 3.10.

1. Tritium-β-decay in the WGTS
   β-decay electrons with an energy distribution $\mathrm{d}N/\mathrm{d}E$ (β-spectrum) are generated in the WGTS. The total number of electrons generated in the WGTS is

$$N_{\mathrm{WGTS}} = \int_{0\,\mathrm{keV}}^{18.6\,\mathrm{keV}} \frac{\mathrm{d}N}{\mathrm{d}E}\mathrm{d}E, \tag{3.3}$$

   the integral over all energies. Because of their isotropic angel distribution half of these electrons are magnetically guided towards the detector and the other half towards the rear wall (compare 2.2).

2. β-decay electrons that reach the detector
   Not all $N_{\mathrm{WGTS}}/2$ β-decay electrons that start in the WGTS towards the detector reach their goal. All those with an initial angle larger than 5° (in scenario 1) are magnetically reflected latest at the pinch magnet. They propagate back towards WGTS and rear wall. The transmission probability depends on the magnetic field in the WGTS $B_{\mathrm{ini}}^{\mathrm{WGTS}}$ (compare equation 2.3)

$$P_{\mathrm{trans}}^{\mathrm{WGTS}} = \frac{1}{2}\cdot(1-\cos\Theta_{\mathrm{max}}) = \frac{1}{2}\cdot\left(1-\sqrt{1-\frac{B_{\mathrm{ini}}^{\mathrm{WGTS}}}{B_{\mathrm{max}}}}\right). \tag{3.4}$$

   This transmission probability only includes magnetic reflection, caused by the increase of the magnetic field on the way to the detector. Any other effects that could influence the electrons on the way, such as non-adiabatic transport, are not included.
   The total number of electrons that reach the detector from the WGTS is

$$N_{\mathrm{det}}^{\mathrm{WGTS}} = \frac{N_{\mathrm{WGTS}}}{2}\cdot P_{\mathrm{trans}}^{\mathrm{WGTS}}. \tag{3.5}$$

   Their energy-distribution is not altered, because the transmission probability is energy independent.

3. β-decay electrons that reach rear wall
   $N_{\mathrm{WGTS}}/2$ β-decay electrons from the WGTS directly head towards the rear wall. They are eventually joined by those that get magnetically reflected on the way to the detector. As the magnetic field consequently drops on the way to the rear wall no electrons get reflected in that direction. The amount of electrons that reach the rear wall is

$$N_{\mathrm{RW}} = \frac{N_{\mathrm{WGTS}}}{2} + (1 - P_{\mathrm{trans}}^{\mathrm{WGTS}}) \cdot \frac{N_{\mathrm{WGTS}}}{2} = N_{\mathrm{WGTS}} - N_{\mathrm{det}}^{\mathrm{WGTS}}. \tag{3.6}$$

   Again their energy distribution remains unchanged, a tritium β-decay spectrum arrives at the rear wall.

4. Backscattering of electrons on the rear wall
   Backscattering causes an energy and angular change of the incoming electron. The β-decay spectrum transforms into a backscatter spectrum. This transformation was simulated with GEANT4. The backscatter probability P_{back} for electrons depends on their energy and impact angle. The number of electrons after backscattering (with a backscatter probability for electrons with β-decay energy spectrum) is

$$N_{\mathrm{RW}}^{\mathrm{back}} = N_{\mathrm{RW}} \cdot P_{\mathrm{back}}. \tag{3.7}$$

   These all start propagating towards the detector.

5. Backscattered electrons that reach the detector
   Because of magnetic reflection not all backscattered electrons reach the detector. The transmission probability is

$$P_{\mathrm{trans}}^{\mathrm{RW}} = 1 - \cos\Theta_{\mathrm{max}} = 1 - \sqrt{1 - \frac{B_{\mathrm{ini}}^{\mathrm{RW}}}{B_{\mathrm{max}}}}, \tag{3.8}$$

   with the magnetic field at the rear wall $B_{\mathrm{ini}}^{\mathrm{RW}}$. Here it was not included, that not all field-lines hit the surface perpendicular[4]. Also an isotropic angle distribution up to angles of 90° to perpendicular for backscattered electrons is assumed.
   Only

$$N_{\mathrm{det}}^{\mathrm{RW}} = N_{\mathrm{RW}}^{\mathrm{back}} \cdot P_{\mathrm{trans}}^{\mathrm{RW}} \tag{3.9}$$

   backscattered electrons reach the detector, with an unchanged backscatter energy distribution.

To compare the spectra as in figure 3.11 for the Au-high case is a vivid way to look at the influence of backscattering. However to get meaningful values on the impact of backscattering it is better to look at the ratio R of the spectrum including backscattering $\mathrm{d}N_{\mathrm{det}}^{\mathrm{tot}}/\mathrm{d}E$ divided by the spectrum excluding the effect $\mathrm{d}N_{\mathrm{det}}^{\mathrm{WGTS}}/\mathrm{d}E$:

$$R = \frac{\frac{\mathrm{d}N_{\mathrm{det}}^{\mathrm{WGTS}}}{\mathrm{d}E} + \frac{\mathrm{d}N_{\mathrm{det}}^{\mathrm{RW}}}{\mathrm{d}E}}{\frac{\mathrm{d}N_{\mathrm{det}}^{\mathrm{WGTS}}}{\mathrm{d}E}} - 1. \tag{3.10}$$

This ratio states, how much the initial spectrum is deviated by the influence of backscattering. For the Au-high case this ratio can be seen in figure 3.12.
A possible way to describe the impact of backscattering is to name how much the spectrum is maximal distorted. The figure shows, that the highest derivation is reached for low energies.

[4] The acceptance angle leading to a certain transmission probability always is the angle relative to the magnetic field lines. For a non-isotropic angle distribution of backscattered electrons, the fact that the field lines do not hit the surface perpendicular leads to a different transmission probability, as their backscatter angle is relative to the surface.

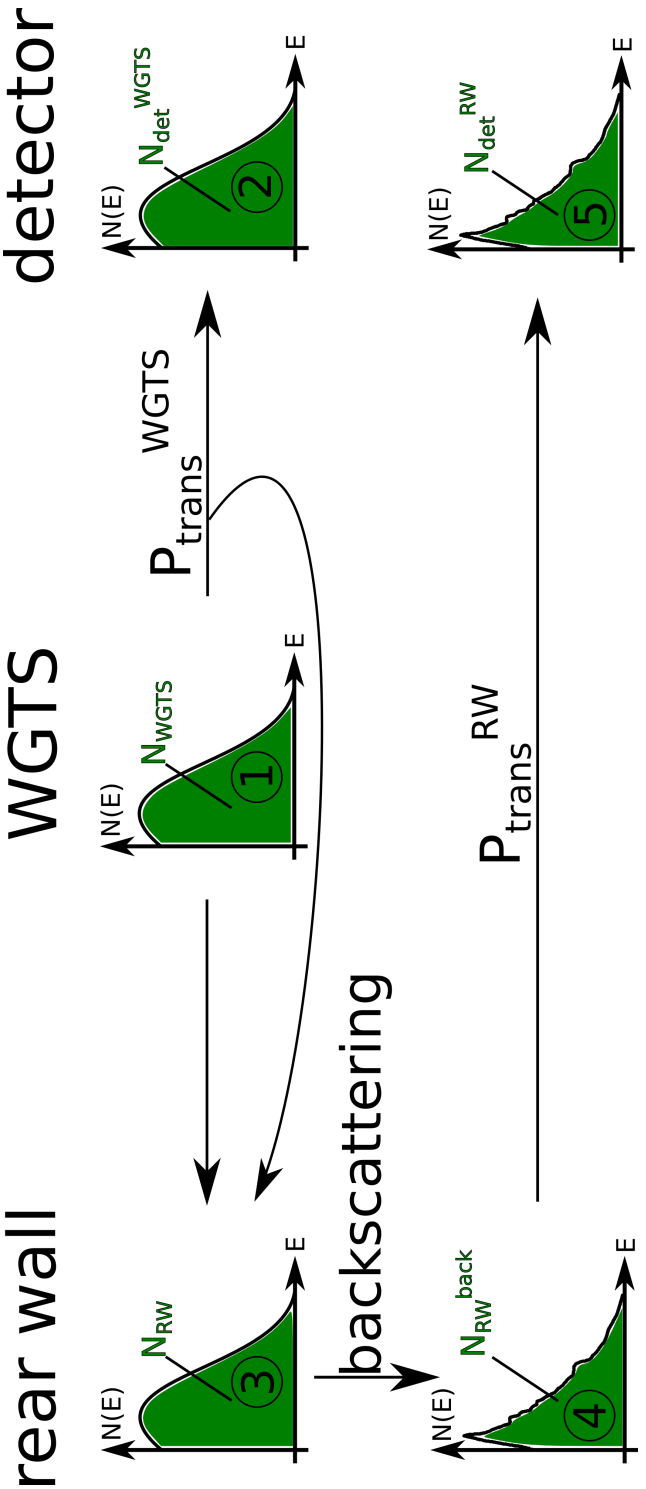


Figure 3.10.: Visualization of the steps listed in 3.3. It is shown how the overall backscatter spectrum at the detector was simulated/calculated.

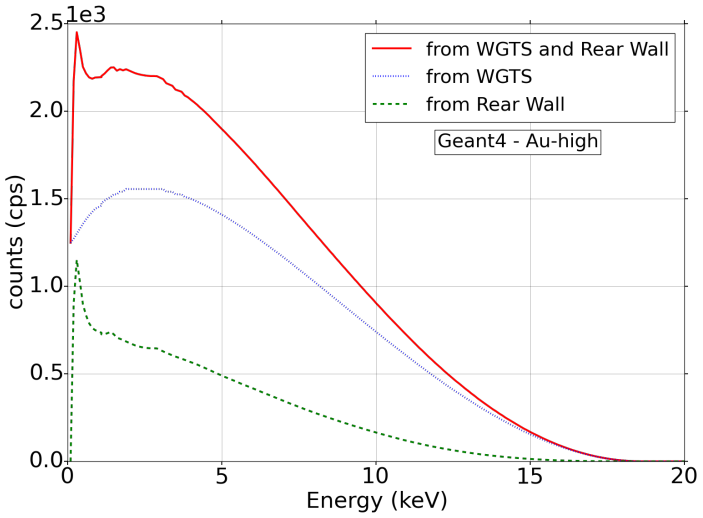


Figure 3.11.: Au-high: The red (drawn through line) shows the spectrum that would be measured at the detector including rear wall backscattering. It is the sum of tritium spectrum coming from the WGTS (blue, dotted) and the backscatter spectrum from the rear wall (green, dashed).The measured spectrum is severely distorted by the influence of backscattering on the rear wall.

3.3.1. Results for scenario 1

For all cases (see figure 3.1) the above calculatations lead to the spectra presented in the following paragraphs.
In all scenario 1 cases the numbers $N_{\mathrm{det}}^{\mathrm{WGTS}}$ and N_{RW} remained unchanged. This means that all spectra would be measured at the detector if all electrons within the sensitive flux tube encountered the conditions listed in table 3.1 (rear wall material, magnetic field). Actually for the low field cases different impacts for different detector rings would needed to be calculated. However, the aim of this thesis is to get an idea of the pros and cons for the different scenarios to be able to decide on the best setting.

Gold rear wall + high magnetic field: Au-high

The spectra in figure 3.11 shows the distortion through backscattering of the measured spectrum. In blue (dotted) the spectra coming from the WGTS, being the one that is supposed to be measured. The backscatter spectrum coming from the rear wall in green (dashed) is the unwanted background. The actually measured spectrum in red is the sum of both. Obviously the measured spectrum gets severely distorted by the influence of rear wall backscattering.
Figure 3.12 shows that for very low energies a maximum derivation of almost 90% is caused by backscattering. The actually measured count rate at these energies is almost twice as high as the intended count rate of the β-decay spectrum.

Gold rear wall + reduced magnetic field: Au-low

With a lower magnetic field at the rear wall the probability for backscattered electrons to reach the detector is decreased. Hence the influence of backscattering is smaller. Figure 3.13 shows that for higher energies the distortion is hardly visible. At low energies only a maximum derivation of 4.1% is reached. The energy dependent ratio can be found in the appendix B.1, there also the results for all scenarios are summarized.
For low magnetic fields not only the gold rear wall plate is hit. Outer flux tube regions

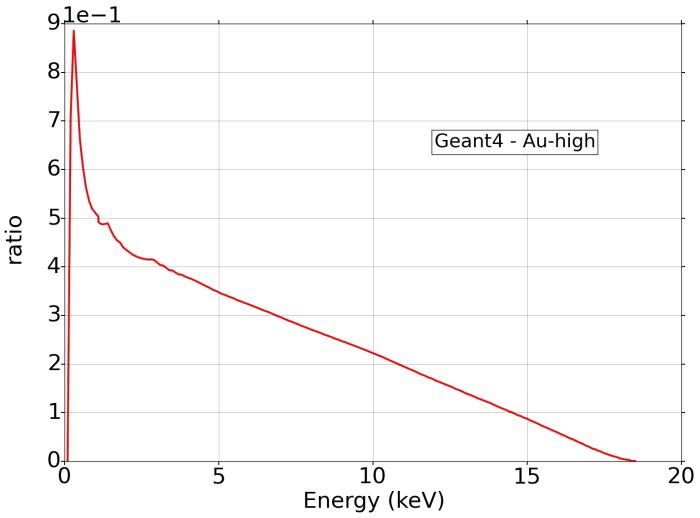


Figure 3.12.: Au-high: Ratio of measured spectrum with and without backscattering on the rear wall. Here the spectrum experiences a maximum derivation of almost 90% at low energies.

(and hence detector rings) deal with the influence of stainless steel backscattering. The size of this influence (reaching from cases SS-low to SS-high) are listed in table 3.2 and the corresponding spectra can be seen in the appendix B.1.
The results for Au-low shown in figure 3.13 only show the influence for the spectrum measured with the innermost detector surface (about 1/3 of the total surface).

Beryllium rear wall + high magnetic field: Be-high

With a much better backscatter behavior, beryllium is the favored rear wall material. Figure 3.14 shows that the distortion is hardly visible for all energies. The maximum derivation is 0.75%.

Beryllium rear wall + reduced magnetic field: Be-low

The lowest influence is reached when combining a beryllium rear wall with a low magnetic field. In figure 3.15 the derivation is again hardly visible. The maximum derivation of 0.26% reaches the aimed sensitivity of the order of 10^{-3}. Because of the low magnetic field again not only the rear wall plate but also the rear wall chamber is hit. As the beryllium plate has a larger radius than the gold plate, here 2/3 of the detector surface measures a spectrum that profits both from the beryllium and low field.

3.3.2. Result for scenario 2

In scenario 2 a lower tritium density in the source is used to reduce the influence of backscattering. For a gold rear wall in a magnetic field that focuses the flux tube on the rear wall plate, the distortion shown in figure 3.16 was calculated. The improvement is much less than expected. In comparison to 90% for the corresponding scenario 1 case, here a maximum derivation of 80% is caused by backscattering.
Because of the higher source magnetic field the overall flux is much higher (see equation 2.2). Table 3.1 shows that a much higher field is needed to focus the whole flux tube on the rear wall plate. Hence also the transmission probability to the detector is increased significantly. The higher transmission probability almost completely overrides the advantage of a lower source strength.
For this and all other cases the results are summarized in table 3.2. The energy dependence of the ratio and the most important facts for all cases can be found in the appendix B.1.

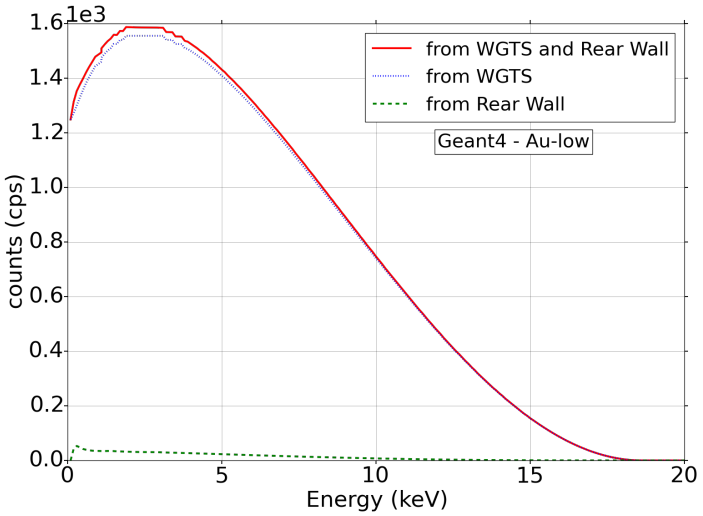


Figure 3.13.: Au-low: The red (drawn through line) shows the spectrum that would be measured at the detector including rear wall backscattering. It is the sum of tritium spectrum coming from the WGTS (blue, dotted) and the backscatter spectrum from the rear wall (green, dashed). The measured spectrum is significantly less distorted than for a higher magnetic field at the rear wall.

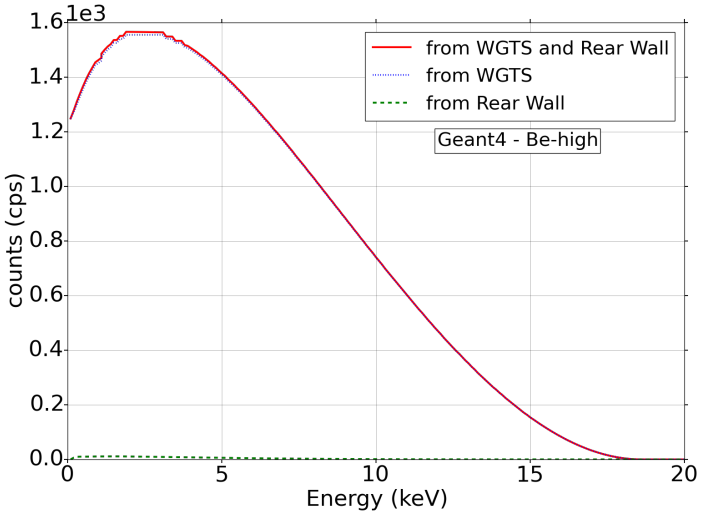


Figure 3.14.: Be-high: The red (drawn through line) shows the spectrum that would be measured at the detector including rear wall backscattering. It is the sum of tritium spectrum coming from the WGTS (blue, dotted) and the backscatter spectrum from the rear wall (green, dashed). The measured spectrum is significantly less distorted than for a gold rear wall plate.

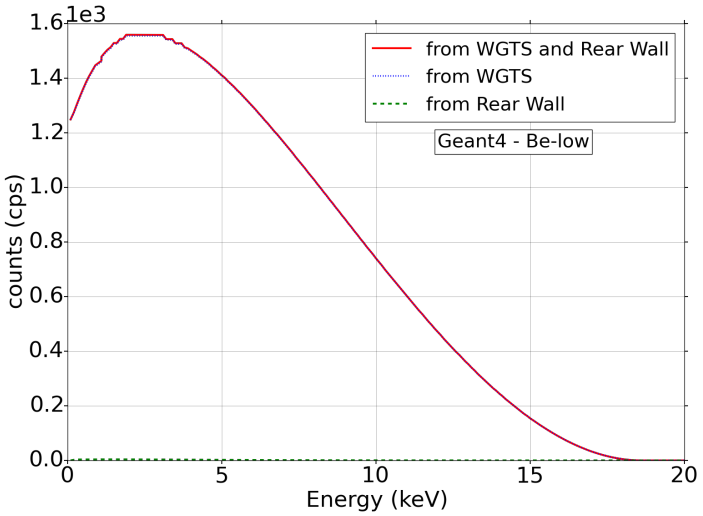


Figure 3.15.: Be-low: The red (drawn through line) shows the spectrum that would be measured at the detector including rear wall backscattering. It is the sum of tritium spectrum coming from the WGTS (blue, dotted) and the backscatter spectrum from the rear wall (green, dashed). The measured spectrum is less distorted than for a higher magnetic field at the beryllium rear wall.

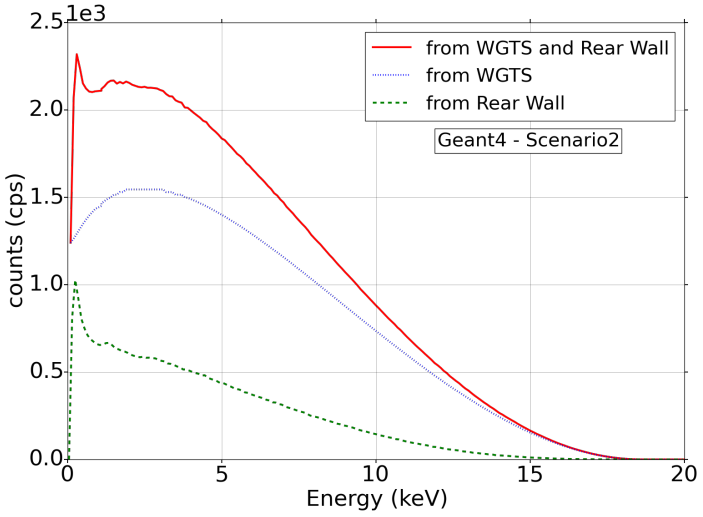


Figure 3.16.: Scenario 2: The red (drawn through line) shows the spectrum that would be measured at the detector including rear wall backscattering. It is the sum of tritium spectrum coming from the WGTS (blue, dotted) and the backscatter spectrum from the rear wall (green, dashed). The measured gets spectrum severely distorted. Only a small improvement compared to scenario 1 (Au-high) is reached.

Table 3.2.: Results from GEANT4 simulations. Backscatter probability P_{back} and probability for the production of an Auger electron P_{Auger}. The spectral distortion is given as maximum from the ratio in equation 3.10. This maximum is reached at low energies.

	Scenario 1						Scenario 2
	Au-high	Au-low	Be-high	Be-low	SS-low	SS-high	
P_{back} (%)	46	43	2		26	26	46
P_{Auger} (%)	< 0.2	< 0.2	0	0	< 0.6	< 0.6	< 0.2
distortion (%)	90	4.1	0.75	0.26	2.4	10	80

4. Conclusion

Due to its outstanding properties, the physics reach of KATRIN can be extended to search for sterile neutrinos in the keV mass range. To cover a wide parameter space, the entire tritium β-decay spectrum is of interest. Hence, new challenges occur. One of the major systematic effects for a keV-scale sterile neutrino search with KATRIN is the backscattering of electrons at the rear wall of the experiment. This thesis introduced the effect, discussed various countermeasures and calculated its impact on the tritium β-decay spectrum using detailed KASPER and GEANT4 simulations. In chapter 2, different scenarios concerning the material and conditions of the rear wall, were introduced and compared. At the end, a suggestion on the material, position and magnetic field at the rear wall was given.

The investigations revealed the following results:

1. Different rear wall materials, i.e, the nominal case of a gold rear wall, stainless steel and beryllium were investigated. The probability for backscattering, meaning elastic scattering with a high angular change, is higher for materials with a high atomic number. For materials such as beryllium ($Z = 4$), with a very low atomic number, only few electrons get backscattered. Hence a beryllium rear wall plate is the favored material. Because the beryllium rear wall plate would have a larger radius than the gold rear wall, as it would be installed in the rear wall chamber, it holds another advantage. A larger flux tube is allowed and therefore a lower magnetic field can be applied.

2. The magnetic field configuration was optimized to minimize the probability of electrons from the rear wall to reach the detector. For low magnetic fields at the rear wall only backscattered electrons with very small angles relative to the magnetic field manage to reach the detector. All others are magnetically reflected. Hence scenarios with a low magnetic field at the rear wall are favored.

3. Finally, different column densities were considered. Generally, of all electrons emitted in the WGTS some fraction reaches the detector while all others will hit the rear wall. By reducing the column density, and increasing the acceptance angle at the same, the rate of electrons at the detector stays the same, while the relative fraction of electrons hitting the rear wall can be reduced. In this thesis it was shown that no significant improvement can be achieved in this scenario.
   On the one hand the effect of backscattered electrons is reduced, but on the other hand, the larger acceptance angle also leads to a larger transmission probability of backscattered electrons to the detector. Hence the two effects cancel and lead to no improvement.

All results for the different scenarios can be found in the tables 3.1 and 3.2.
In summary, it was demonstrated that in case of the nominal KATRIN scenario (gold rear

wall, high magnetic field) the effect of rear wall backscattering can be as large as 90%. Hence not acceptable for a sterile neutrino search. The best scenario was identified to be the usage of a beryllium rear wall in combination with a low magnetic field. In this case the effect on the final spectrum is reduced to 0.26%.
The simulations performed in this thesis apply to the case of a first sterile neutrino search with KATRIN during the commissioning phase. In the framework of the TRISTAN project a second phase with a new detector system and the full KATRIN statistics is planned. The results presented in this thesis lay the crucial ground work for designing an optimal rear wall and magnetic field layout for this high-sensitivity sterile neutrino search with KATRIN.

Appendix

A. KASPER simulations

A.1. Calculation of the safety margin for Au-high

To focus the whole flux of $1.73\,\mathrm{T\,cm^2}$ on the gold rear wall with a radius of $r_{\mathrm{RW}} = 7.5\,\mathrm{cm}$, a field of 98 G is needed. However as already discussed in section 2.2 the cyclotron motion of the electrons needs to be considered. The flux tube needs to be compressed such that the cyclotron radius is smaller than the distance of the flux tube to the edge of the rear wall plate.
For a magnetic field of $B_{\mathrm{RW}} = 165\,\mathrm{G}$ the flux tube has a radius of (compare equation 2.2)

$$r_{\mathrm{flux}} = \sqrt{\frac{\Phi}{B_{\mathrm{RW}} \cdot \pi}} \approx 5.8\,\mathrm{cm},$$

leaving a 1.7 cm safety margin to the edge of the rear wall.
Equation 2.1 states, that the cyclotron radius also depends on the kinetic energy of the electron perpendicular to the magnetic field. As electrons have a maximum impact angle on the rear wall (see equation 1.13) this component needs to be calculated. β-decay electrons do not possess energies above $E_0 = 18.6\,\mathrm{keV}$. Hence the maximum perpendicular energy is

$$E_\perp = \sin\Theta_{\mathrm{imp}}^{\mathrm{max}} \cdot E_0 = \sqrt{\frac{B_{\mathrm{RW}}}{B_{\mathrm{WGTS}}}} \cdot E_0 \approx 11.3\,\mathrm{keV}.$$

According to equation 2.1 this energy causes a cyclotron radius of $r_{\mathrm{L}} = 2.2\,\mathrm{cm}$. A field of at least 183 G would be needed to make the safety margin bigger than the cyclotron radius. Since high fields cause an increased transmission probability and only very few electrons actually are created with the endpoint energy E_0, the 165 G will here be considered to hold a high enough safety margin.
The field at the rear wall is a superposition of the stray fields from the DPS1R and WGTS-magnets as well as the RSCM-main-magnets (compare figure 3.2). To generate a certain field at the rear wall the currents of RSCM-main are changed according to

$$I_{\mathrm{f}} = I_{\mathrm{i}} \cdot \frac{B_{\mathrm{RW}}}{B_{\mathrm{i}}}. \tag{A.1}$$

Where I_{i} and B_{i} are the current in the solenoids in normal KATRIN-mode and the magnetic field generated at the rear wall with that current. B_{RW} is the intended rear wall field. Because there is no magnet directly around the rear wall the magnetic field is not constant on the whole rear wall surface. The actual mean magnetic field resulting from the current in equation A.1 is therefore not the exact same as the intended B_{RW}.

A.2. Parameters and results for other scenarios

Au-low

In the Au-low case all rear section magnets in figure 3.2 are turned off, leaving the lowest possible field at the rear wall, the stray field from WGTS and DPS1R magnets. The

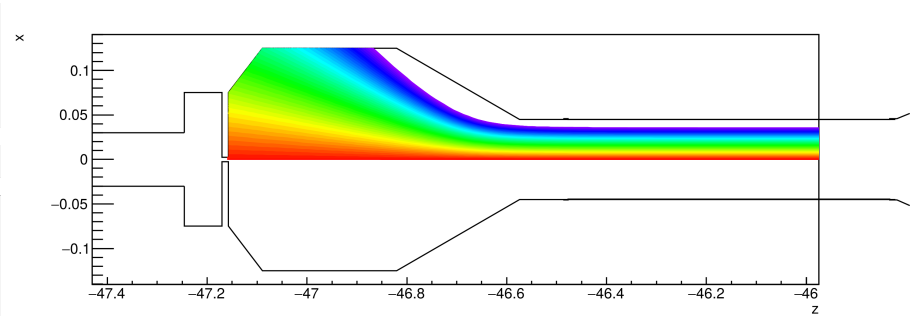


Figure A.1.: Au-low: Rear wall chamber with electron trajectories coming from the WGTS. The color represents their initial radius. The rainbow colored area corresponds to the total sensitive flux tube. The different hit walls are represented in figure A.2 by lines with different slopes

electron trajectories and points of impact can be seen in figure A.1. The flux tube is that broad that also the walls around the rear wall are hit. Electrons that do not hit the rear wall plate backscatter on stainless steel. Figure A.2 shows the magnetic field for different radii. When comparing figures A.1 and A.2 one can see that the course of the magnetic field mirrors the geometry of the rear wall chamber. Each wall segment (rear, tilted and horizontal wall) is represented by a straight line with a certain slope.
Au-low only considers electrons that hit the rear wall plate, all these electrons undergo a mean magnetic field of $\bar{B}_{\mathrm{imp}} \approx 8.37\,\mathrm{G}$. They correspond to about 1/3 of the total flux tube. Hence the shown results only apply for electrons detected in the inner detector rings. Nevertheless, the following simulations treated Au-low as if all electrons within the sensitive flux tube encountered the conditions on the rear wall plate. This does not change the overall calculated impact.
Stainless steel is hit close to the rear wall up to points way further towards the WGTS. Because the stray field from the WGTS is much higher there the field on the stainless steel walls varies from 8.26 G to 33.86 G. To gain an idea of the influence of stainless steel backscattering two scenarios will be considered. In the 'SS-low' scenario all electrons within the sensitive flux tube will hit a stainless steel wall in a field of 8.26 G. For 'SS-high' in a field of 33.86 G.
The corresponding maximum impact angles $\Theta_{\mathrm{imp}}^{\mathrm{max}}$ and transmission probabilities $P_{\mathrm{trans}}^{\mathrm{RW}}$ for all three cases are listed in table 3.1.

Be-high and Be-low

Figure 2.8 shows where a beryllium rear wall with a radius of $r = 12.5\,\mathrm{cm}$ would be installed. To stop electrons at the beryllium wall the terminator 'min_z' was used. As the beryllium sits at $z = -47$ in KASPER coordinates, tracking of electrons stopped when their z position fell below that value. However KASPER is not very precise when stopping electrons at a certain coordinate. Depending on their step size the electrons exceed the aimed values by different ranges. The reason is that they are terminated after their actual position is higher than the aimed (at the end of a step). For termination on geometry walls the electrons are tracked until their position is exactly the one of the wall.
The result of these different termination definitions can be seen in figure A.3, showing the electron trajectories. Figure A.4 shows that the 'two late' termination of some electrons of course also leads to a rough course of the determined magnetic field. It was also tried to extract information on the magnetic field at the position $z = -47$ by using the step output from KASPER simulations. This means after propagating electrons further than the beryllium wall the magnetic field at around -47 was extracted. But since the simulation-steps were not altered the same step like behavior was found.

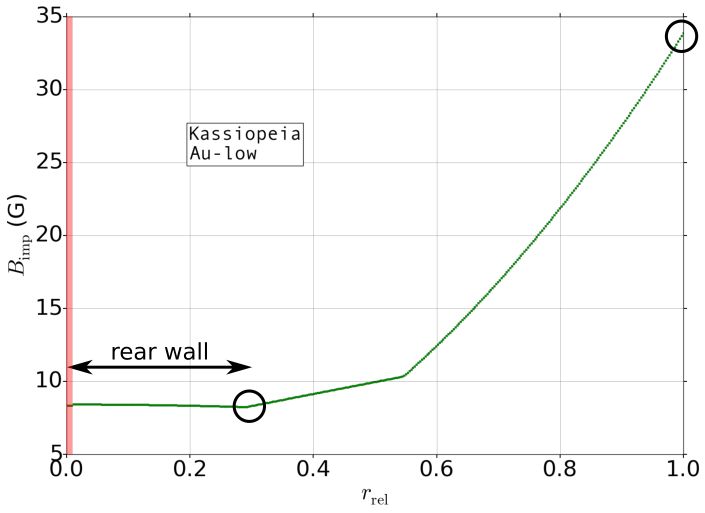


Figure A.2.: Au-low: Total magnetic field at the point of impact of an electron on the rear wall plate and the rear wall chamber walls B_{imp} versus the relative flux tube radius of the electron r_{rel}. The impact of the backscattering on the rear wall and of two different points of the stainless steel walls (black circles, scenarios SS-low and SS-high) will be investigated with GEANT4.

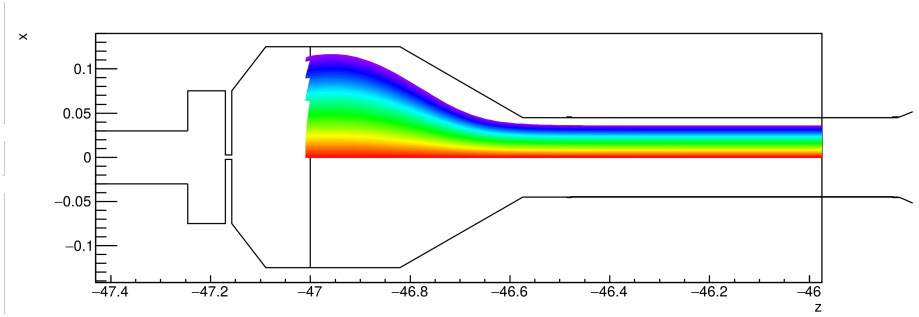


Figure A.3.: Be-high: Rear wall chamber with electron trajectories coming from the WGTS. The color represents their initial radius. The rainbow colored area corresponds to the total sensitive flux tube. As described in the text the electrons are not nicely terminated at the surface of the beryllium wall but after exceeding a position of $z = -47$.

The only possibility to get exact information about the field at the beryllium wall would be to alter the geometry of the rear wall chamber. Here however the information gained by using a terminator is considered to be sufficient.
If the flux tube is focused on the wall ('Be-high') as shown in figures A.3 and A.4 the electrons encounter magnetic fields of a little more than 44 G. When turning off all rear section magnets ('Be-low', figures A.5 and A.6) the electrons encounter fields of a little more than 16 G. Then again the impact of backscattering on stainless steel must be taken into account for the outer detector rings. However for a beryllium rear wall more than 2/3 of the sensitive flux tube actually illuminates it, much more than for the gold wall in the low-field case. Here already a great advantage of the beryllium wall is clear. As is has a much higher radius than the gold rear wall the flux tube needs to be much less compressed to fit on it.

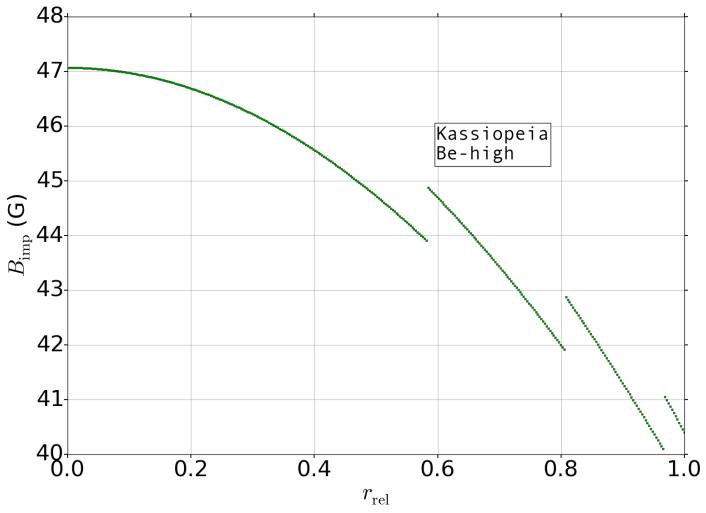


Figure A.4.: Be-high: Total magnetic field at the point of impact of an electron on the rear wall and surrounding walls B_{imp} versus the relative flux tube radius of the electron r_{rel}. The steps in the slope of the magnetic field are caused by a not exact terminations of the electrons at a position of $z = -47$ (see text).

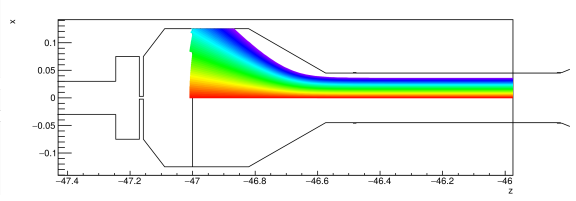


Figure A.5.: Be-low: Rear wall chamber with electron trajectories coming from the WGTS. The color represents their initial radius. The rainbow colored area corresponds to the total sensitive flux tube. As described in the text the electrons are not nicely terminated at the surface of the beryllium wall but after exceeding a position of $z = -47$.

B. GEANT4 simulations

B.1. Summary of all results

For the results from the GEANT4 simulations, including propagation of the backscattered spectrum to the detector, were shown in section 3.3. The below figures B.7 to B.11 summarize the results, including the ratio of the spectrum with and without backscattering (compare equation 3.10). In table 3.2 all values gained from GEANT4 simulations are listed.

B.2. Validation of the GEANT4 monte carlo simulation toolkit

For the investigations concerning rear wall backscattering, explicit also the production of secondary particles such as Auger electrons is of interest. Table 3.2 shows that the impact of these secondary particles is rather small compared to backscattering. But is the GEANT4 monte carlo simulation toolkit really capable of simulating these processes precise enough?
To better understand the capability and function of GEANT4 to simulate Auger electrons this additional investigations were made. Instead of looking at the energy of all reflected and charged particles as done in the previous discussions other outputs can be chosen. Here the energy of secondary particles is of interest. GEANT4 stores the energy they posses at the moment they are generated, meaning they did not experience any energy losses due to

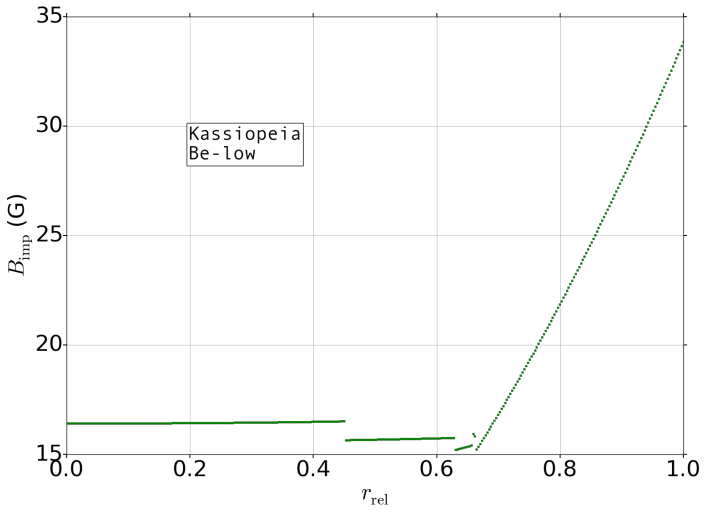
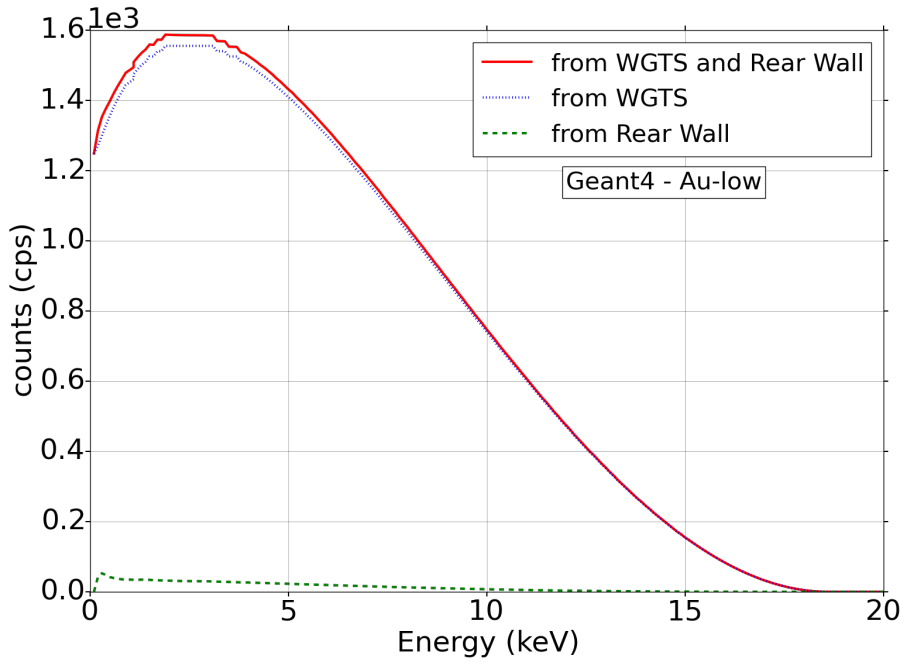
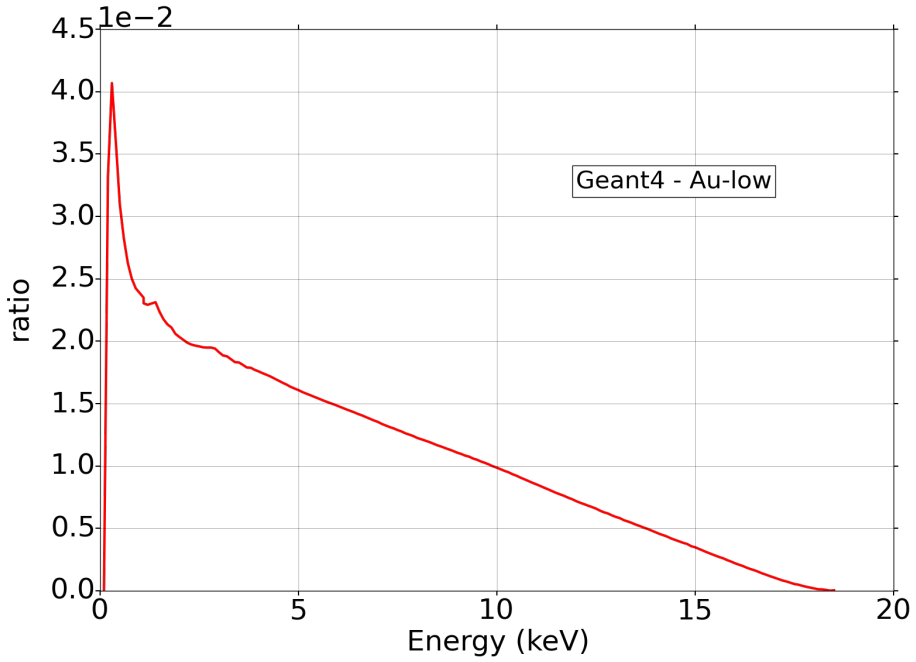


Figure A.6.: Be-low: Total magnetic field at the point of impact of an electron on the rear wall and surrounding walls B_{imp} versus the relative flux tube radius of the electron r_{rel}. For $r_{\mathrm{rel}} > 0.65$ the stainless steel wall of the rear wall chamber vessel is hit (compare figure A.5)

propagation through matter jet.
When 10^7 photons with an energy of 100 keV hit a 1 mm thick gold target, the energy spectrum up to 20 keV of secondary particles is shown in figure B.13. The Auger lines described in section 2.3 can be seen.
In [I+16] the capability of GEANT4 to simulate the production of Auger electrons was investigated. In particular the improvements made on the Auger cascade for the version 10.1 release were compared to older versions. Figure B.14 shows the simulated Auger lines. In the paper the target consists of 10 nm gold nano-particles that is hit by 100 keV photons. Unfortunately the exact target geometry is not described. Because of the atomic shell structure of gold only three energy ranges are of interest when looking at Auger electrons. They are the ones shown in figure B.14.

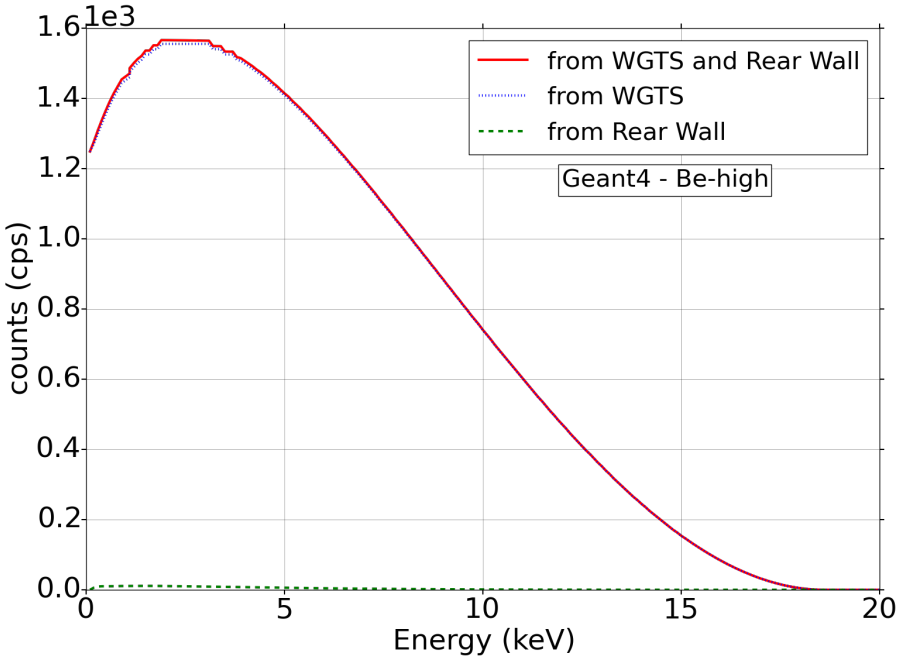


(a) Spectra at detector

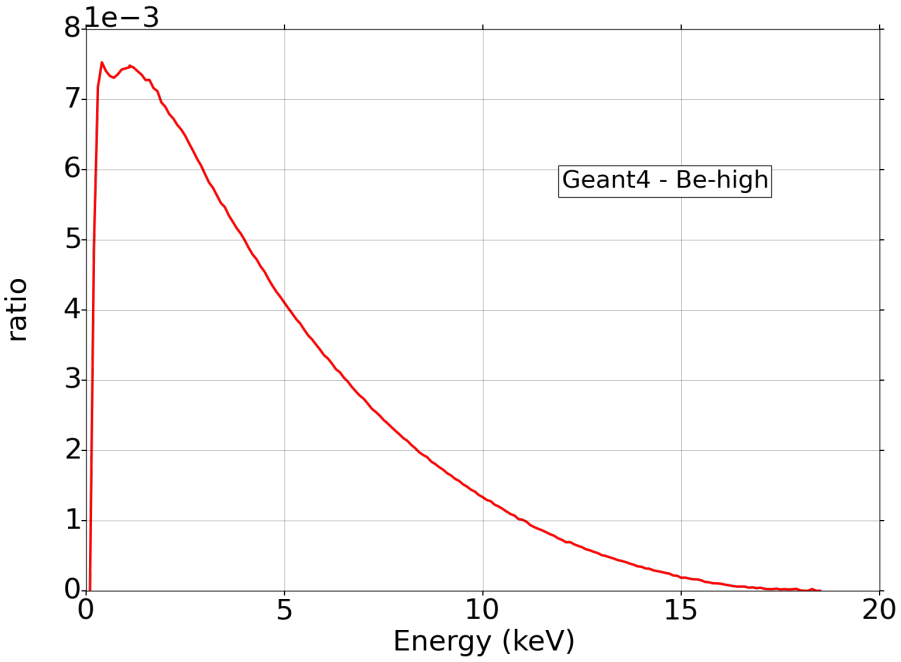


(b) Ratio

Figure B.7.: Au-low: Figure B.7a shows the spectrum that would be measured at the detector when rear wall backscattering is included (red, drawn through line). It is the sum of the intended tritium spectrum coming from the WGTS (blue, dotted) and the backscatter spectrum from the rear wall (green, dashed). In figure B.7b the ratio of the spectrum with and without backscattering, as defined in equation 3.10, can be seen. It states that the spectrum gets maximal distorted by 4.1%.
Compared to the spectra shown in figure 3.11 the influence of backscattering is much smaller. Because of the lower magnetic field at the rear wall much less backscattered electrons manage to reach the detector. However only about 1/3 of the sensitive flux tube actually hits the rear wall (see figure A.1). The above results only apply for the spectrum measured with the inner detector rings. For the outer detector rings the backscattering on stainless steel must be taken into account. Its influence is shown in figures B.10 and B.11.

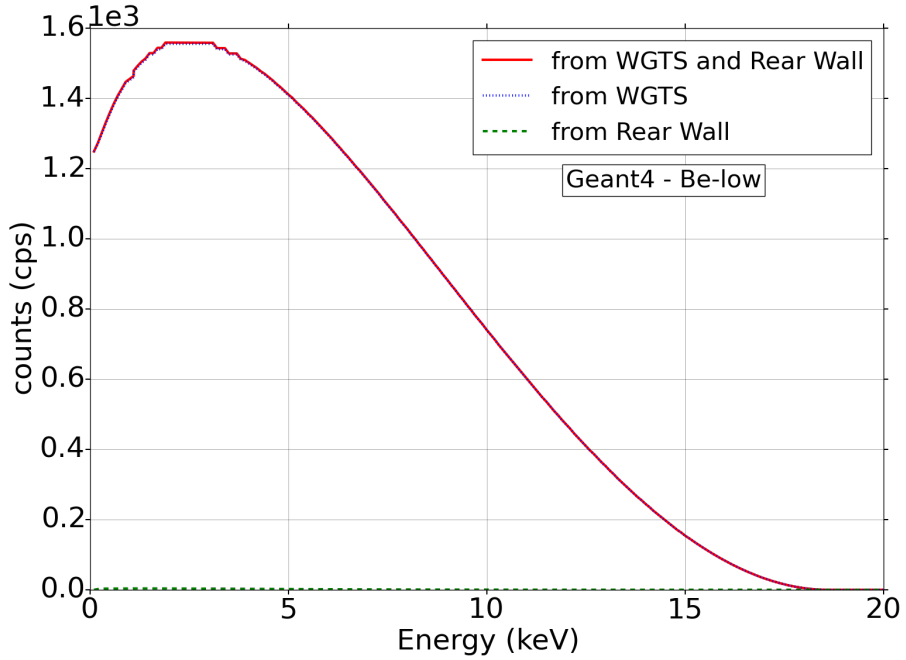


(a) Spectra at detector

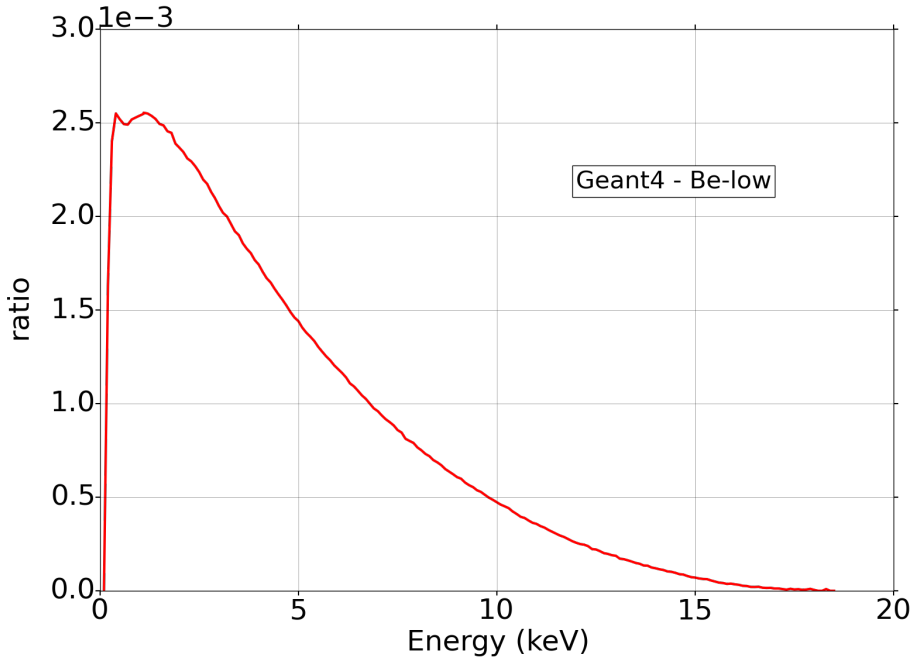


(b) Ratio

Figure B.8.: Be-high: Figure B.8a shows the spectrum that would be measured at the detector when rear wall backscattering is included (red, drawn through line). It is the sum of the intended tritium spectrum coming from the WGTS (blue, dotted) and the backscatter spectrum from the rear wall (green, dashed). In figure B.8b the ratio of the spectrum with and without backscattering, as defined in equation 3.10, can be seen. It states that the spectrum gets maximal distorted by 0.75%.
Here the spectrum gets much less distorted as for the gold rear wall cases. The two reasons are, that beryllium shows a much better backscatter behavior (compare figure 2.7) and because of the larger radius of the beryllium wall a smaller field is needed to focus the sensitive flux tube on the wall (resulting in a lower transmission probability). To suppress the effect further an even lower field could be applied at the beryllium rear wall. The corresponding results are shown in figure B.9.

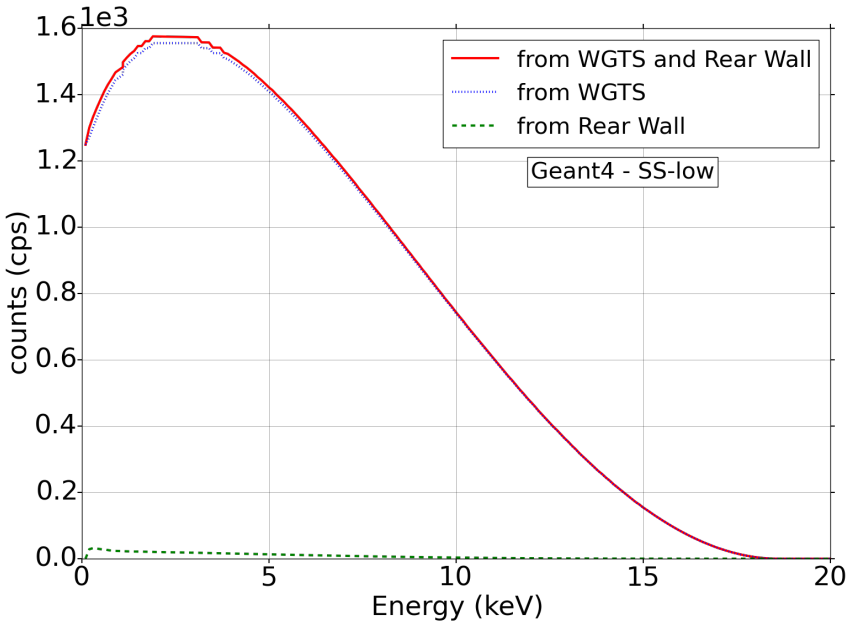


(a) Spectra at detector

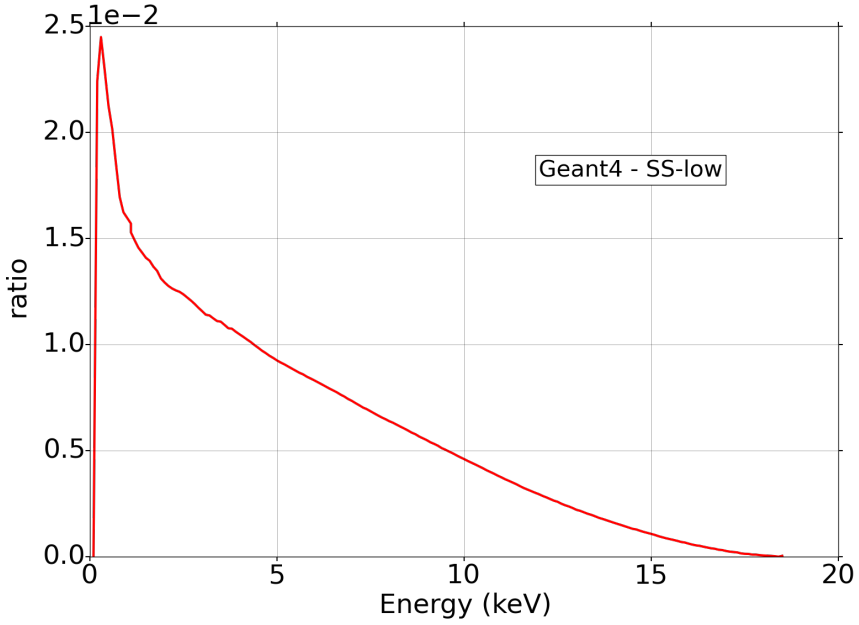


(b) Ratio

Figure B.9.: Be-low: Figure B.9a shows the spectrum that would be measured at the detector when rear wall backscattering is included (red, drawn through line). It is the sum of the intended tritium spectrum coming simulated from the WGTS (blue, dotted) and the backscatter spectrum from the rear wall (green, dashed). In figure B.9b the ratio of the spectrum with and without backscattering, as defined in equation 3.10, can be seen. It states that the spectrum gets maximal distorted by 0.26%.
The lowest possible influence is reach in this scenario. Here the good backscatter behavior of beryllium as well as the lowest possible transmission probability for backscattered electrons come together. However as already mentioned for the Au-low scenario (figure B.7), not the whole sensitive flux tube fits on the wall for such low fields. Hence the above results only apply for 2/3 of the sensitive flux tube. For regions measured with the outer detector rings the influence of stainless steel backscattering needs to be considered (compare figures B.10 and B.11).

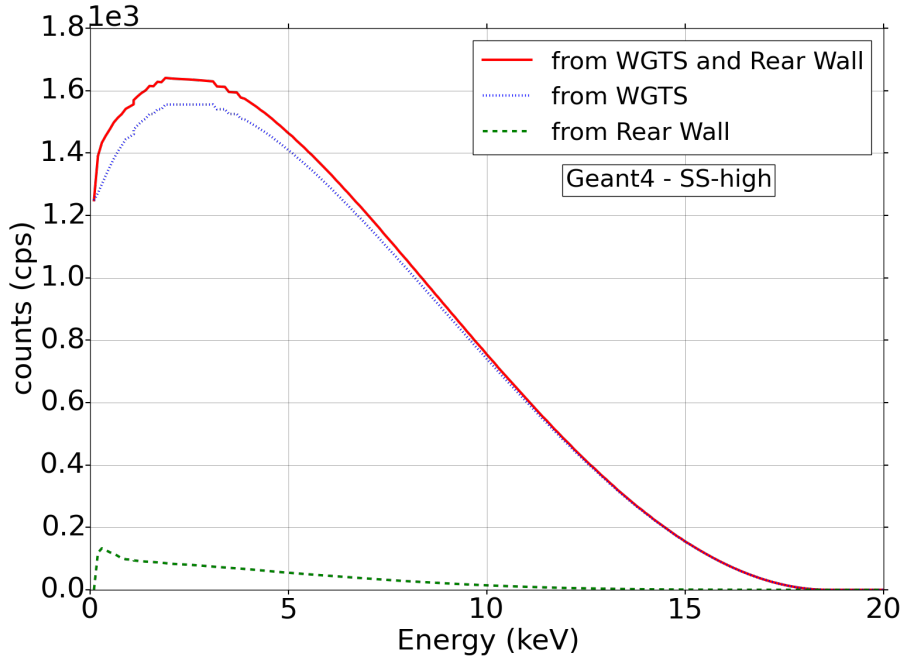


(a) Spectra at detector

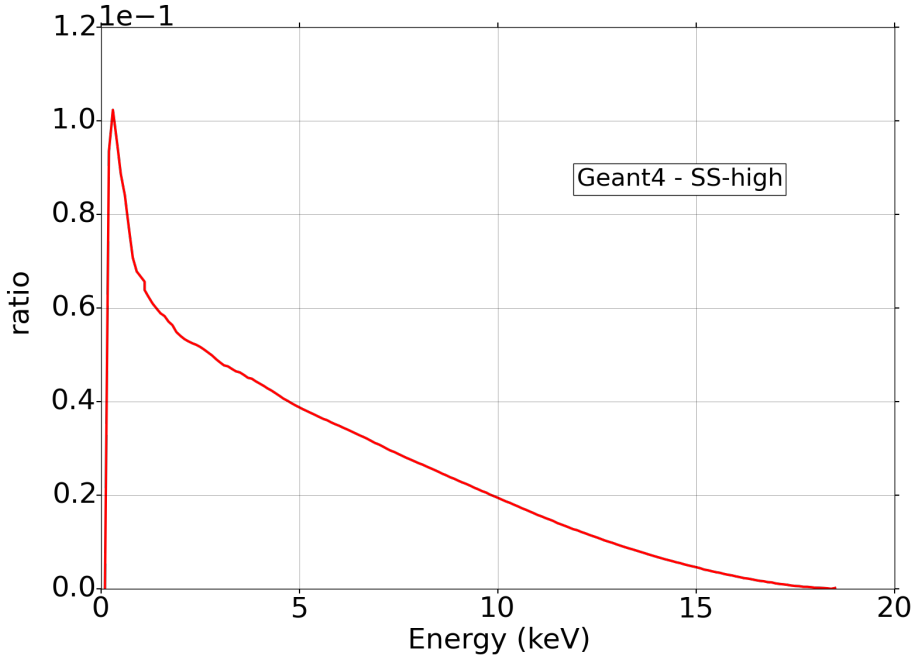


(b) Ratio

Figure B.10.: SS-low: Figure B.10a shows the spectrum that would be measured at the detector when rear wall backscattering is included (red, drawn through line). It is the sum of the intended tritium spectrum coming from the WGTS (blue, dotted) and the backscatter spectrum from the rear wall (green, dashed). In figure B.10b the ratio of the spectrum with and without backscattering, as defined in equation 3.10, can be seen. It states that the spectrum gets maximal distorted by 2.4%.
Backscattering on stainless steel needs to be taken into account when not the whole sensitive flux tube fits on the rear wall because of a too low magnetic field. This happens for the cases Au-low (figure B.7) and Be-low (figure B.9). The above plots show the lowest possible impact of stainless steel backscattering for the gold rear wall. Right next to the edge of the gold rear wall electrons encounter the stainless steel walls of the rear wall chamber in the lowest possible field (furthest away from WGTS). If all electrons within the sensitive flux encountered the conditions that were simulated at this point (compare table 3.1) the above spectrum could be measured at the detector. All influences of stainless steel on the measured spectrum (for Au-low) lie between this case and the results shown in figure B.11. For a beryllium rear wall the lowest possible impact lies between these two cases.

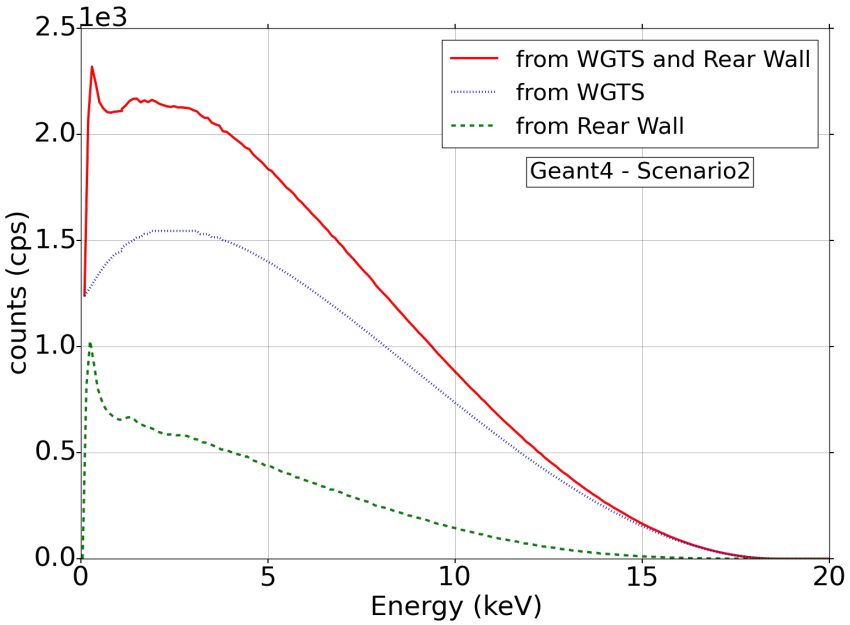


(a) Spectra at detector

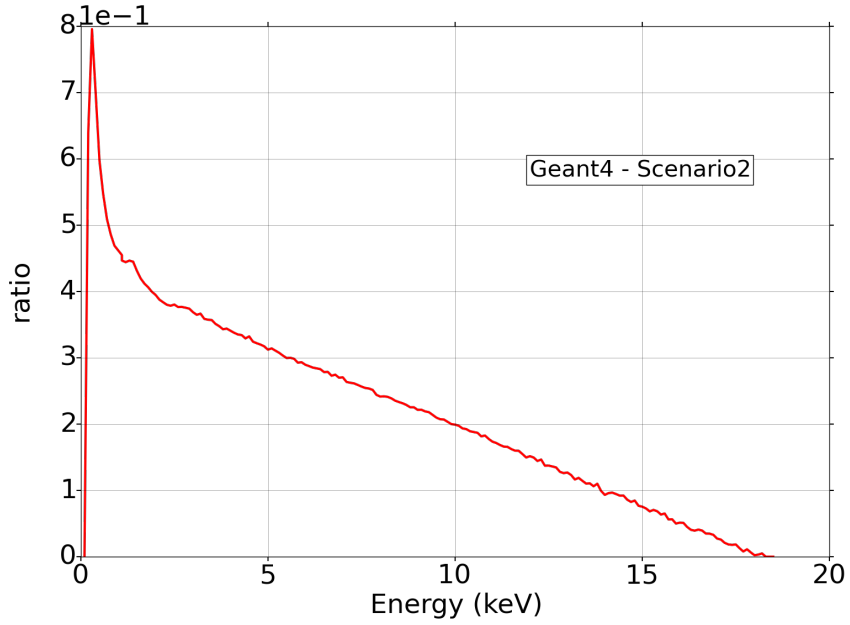


(b) Ratio

Figure B.11.: SS-high: Figure B.11a shows the spectrum that would be measured at the detector when rear wall backscattering is included (red, drawn through line). It is the sum of the intended tritium spectrum coming from the WGTS (blue, dotted) and the backscatter spectrum from the rear wall (green, dashed). In figure B.11b the ratio of the spectrum with and without backscattering, as defined in equation 3.10, can be seen. It states that the spectrum gets maximal distorted by 10%.
Backscattering on stainless steel needs to be taken into account when not the whole sensitive flux tube fits on the rear wall because of a too low magnetic field. This happens for the cases Au-low (figure B.7) and Be-low (figure B.9). The above plots show the highest possible impact of stainless steel backscattering. When comparing figure 3.1 one can see, that for the lowest possible field the flux tube (blue) hits the stainless steel wall up to an outer-right point. If all electrons within the sensitive flux encountered the conditions that were simulated at this point (compare table 3.1) the above spectrum could be measured at the detector.



(a) Spectra at detector



(b) Ratio

Figure B.12.: Scenario 2: Figure B.12a shows the spectrum that would be measured at the detector when rear wall backscattering is included (red, drawn through line). It is the sum of the intended tritium spectrum coming from the WGTS (blue, dotted) and the backscatter spectrum from the rear wall (green, dashed). In figure B.12b the ratio of the spectrum with and without backscattering, as defined in equation 3.10, can be seen. It states that the spectrum gets maximal distorted by 80%.
Scenario 2 was considered because a higher source field leads to much less electrons at the rear wall as compared to the detector. Therefore the effect is not amplified as much as for the other scenarios. However because of the higher overall flux a high magnetic field at the rear wall is needed to focus the sensitive flux tube on the wall. This leads to a much higher transmission probability for backscattered electrons as compared to the other scenarios. The still very high impact on the measured spectrum of 80% states that the advantage of the minimization of the rear wall count rate gets almost completely overridden by the higher transmission probability. Even applying a lower magnetic field at the rear wall (as happed in the Au-low case for scenario 1) would not help. Here even less than 1/3 of the sensitive flux tube would then actually hit the rear wall.

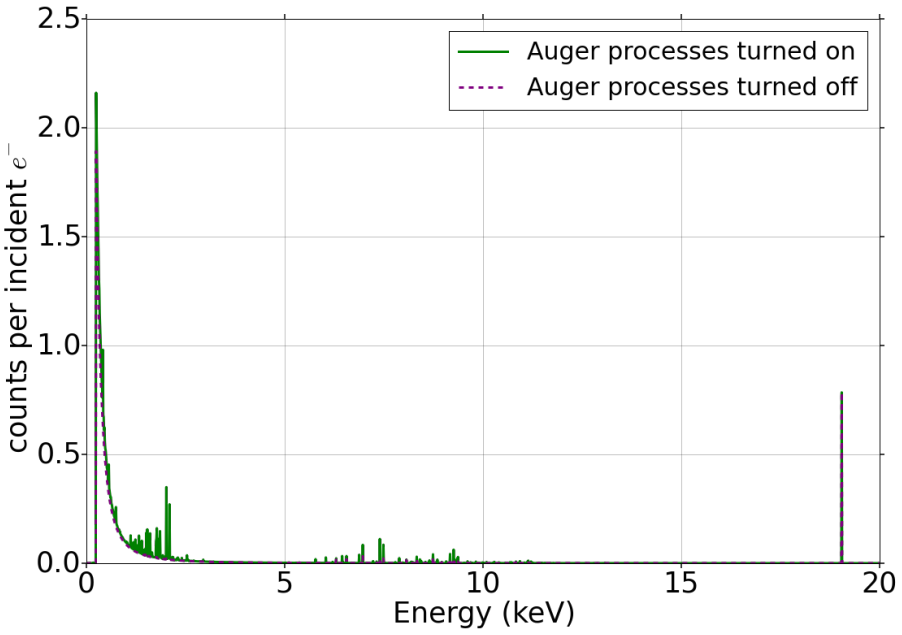


Figure B.13.: Simulated energies of secondary particles created from 100 keV photons in a 1 mm thick gold target. In on simulation (purple, dashed line) all Auger processes were turned off. The lines in the energy ranges from 1 keV to 2.5 keV and 5 keV to 12 keV result from Auger electrons. However the peak at ≈19 keV does not, as it is also simulated without activated Auger processes.

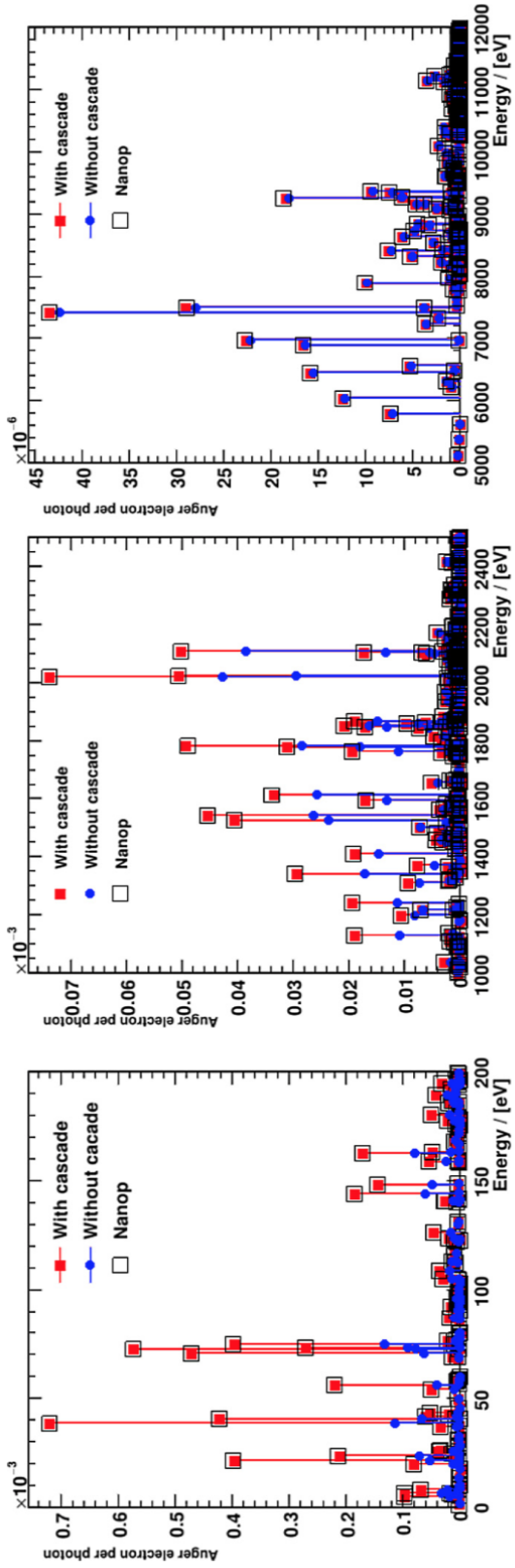
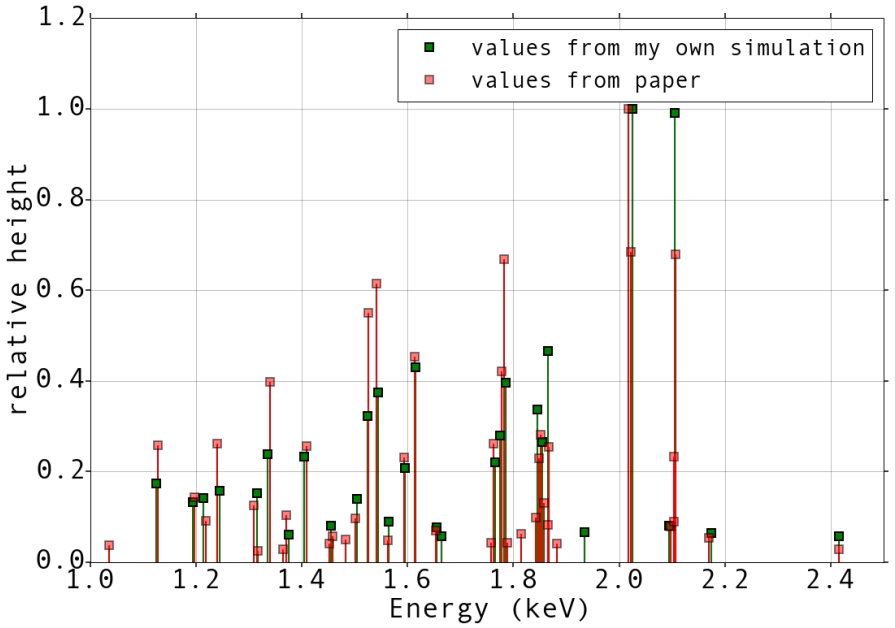


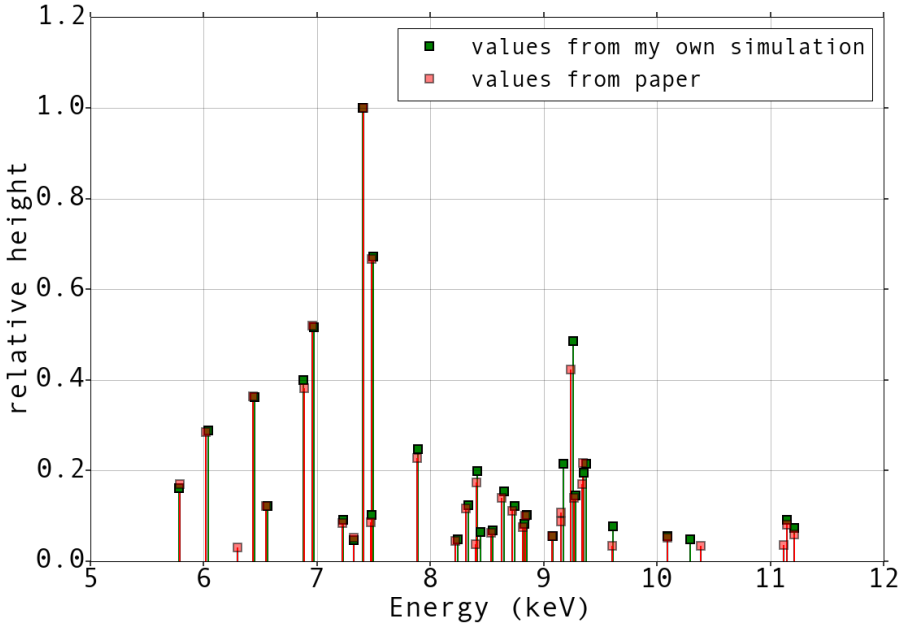
Fig. 11. Comparison of Auger electron emission spectra per incident photon in a 10 nm diameter gold NP, obtained for 2×10^{10} 100 keV incident photons, taking into account (red squares) or not (blue disks) the full simulation of the deexcitation cascade. Three different energy ranges are shown: 0–200 eV (left plot), 1–2.5 keV (middle plot), 5–12 keV (right plot). Results for the full cascade simulation (red squares) are compared to values obtained with the "Nanop" software (empty squares) as described in [14], illustrating the possibility to fully simulate the Auger cascade using Geant4 (from release 10.2 Beta, June 2015). (For interpretation of the references to color in this figure legend, the reader is referred to the web version of this article.)

Figure B.14.: Auger lines gained in the simulations from [I+16]. The lines in energy ranges two and three were reproduced by own simulations (compare figure B.15). Figure from [I+16].

To test the capability of the GEANT4 version and example used for the rear wall investigations the aim is to redo the simulations described in the paper with the same results. Only the later two energy ranges in figure B.14 can be reproduced as the lowest one falls below the minimal considered energy of 250 eV. This minimal energy is defined in the configuration macro for the GEANT4 simulation.
As the exact geometry of the gold nano-particles is not known 10^9 photons were send on a 10 nm thick rectangular gold target. The output (energy of secondary particles at their creation) is written into a histogram with 10 eV bins. It is not possible to only consider Auger electrons (eg. by marking them at creation). To get Auger electrons only the difference between the count-rates with and without activated Auger processes is considered, this is however only an approximation on the actual number of Auger electrons.
As only the Auger lines (position and height) are of interest all bins with low count rates are neglected.
The Auger lines gained by this approach can then be compared to the values from the paper. All heights and positions of the Auger lines in figure B.14 were extracted by using WebPlotDigitizer. Because of the many peaks for low count rates only the values for comparatively large peaks could be extracted.
To make the two data-sets more comparable both are normed by the height of the highest peak, it then has the height 1 all others heights below 1 (compare figure B.15). Both data are then compared in figure B.15.
In the third energy range (from figure B.14) the values from the paper (red) are in very good agreement to the reproduced simulation results (green). This includes position and relative height of the Auger lines. However for the lower energy range large discrepancies can be seen. The position (energy) of the lines seems to fit for most peaks (one red and one green one at the same position). At energies where only red lines can be seen probably the peak from the copied simulation was to small and therefor neglected.
Almost all peaks from the paper are much higher than the replicated. When taking a closer look one can see, that at some energies two red peaks can be seen, when only one green one can be found. This happens for example for the highest peak. One reason for the discrepancies therefore could be, that the binning of the replicated histogram was not small enough and therefore two peaks were counted as one (which is then to high). If that happed for the highest peak that was used as reference height the mostly too small replicated peaks can be explained. Also the simulation geometry was not exactly the same this could be another reason for the deviation.
For high energies (above 5 keV) the values from the paper were reproduced very well. In this ranges a high confidence can be laid on the simulations. For lower energies at least the height of the Auger peaks could not be reproduced. Here the simulated amount of Auger electrons needs to be treated with caution.
To gain further trust in the simulations the comparison with measured backscatter data would be very interesting.



(a) second energy range



(b) third energy range

Figure B.15.: Comparison of the values from figure B.14 with the replicated simulation results. For higher energies a high accordance was reached. Some possible reasons for the discrepancies in the lower energy range are discussed in the text. Most of all a problem with binning needs to be considered.

Bibliography

[A+01] Ahmad, Q. R. *et al.*: *Measurement of the Rate of $\nu_e + d \rightarrow p + p + e^-$ Interactions Produced by ^8B Solar Neutrinos at the Sudbury Neutrino Observatory.* Phys. Rev. Lett., 87:071301, Jul 2001.

[B+16] Bode, T. *et al.*: *Sterile Neutrino search with the First Light of KATRIN.* to be published, 2016.

[BIR12] Boyarsky, Alexey, Dmytro Iakubovskyi und Oleg Ruchayskiy: *Next decade of sterile neutrino studies.* Physics of the Dark Universe, 1:136 – 154, 2012, ISSN 2212-6864.

[BPB01] Bahcall, John N., M. H. Pinsonneault und Sarbani Basu: *Solar Models: Current Epoch and Time Dependences, Neutrinos, and Helioseismological Properties.* The Astrophysical Journal, 555(2):990, 2001.

[CRH+56] Cowan, C.L., F. Reines, F.B. Harrison, H.W. Kruse und A.D. McGuire: *Detection of the Free Neutrino: a Confirmation.* Science, 124:103–104, 1956.

[D+62] Danby, G. *et al.*: *Observation of Hight-Energy Neutrino Reactions of Two Kinds of Netrinos.* Physical Review Letters, 9:36–44, 1962.

[D+16] Drewes, M. *et al.*: *A White Paper on keV Sterile Neutrino Dark Matter*. 2016.

[Dav94] Davis, Raymond: *A review of the homestake solar neutrino experiment.* Progress in Particle and Nuclear Physics, 32:13 – 32, 1994.

[Dol16] Dolde, Kai: *Detector and read-out development to search for sterile neutrinos with KATRIN.* master thesis, KIT, 2016.

[DW94] Dodelson, Scott und Lawrence M. Widrow: *Sterile neutrinos as dark matter.* Phys. Rev. Lett., 72:17–20, Jan 1994. `http://link.aps.org/doi/10.1103/PhysRevLett.72.17`.

[F+98] Fukuda, Y. *et al.*: *Evidence for Oscillation of Atmospheric Neutrinos.* Phys. Rev. Lett., 81:1562–1567, Aug 1998.

[Fer34] Fermi, Enrico: *Versuch einer Theorie der Betastrahlen.* Zeitschrift für Physik, 88:161, 1934.

[Gea] *Official Geant4 homepage.* `geant4.cern.ch`.

[Har12] Harms, F.: *Assembly and First Results of the KATRIN Focal-Plane Detector System at KIT.* Diplomarbeit, KIT, 2012.

[Hub15] Huber, Anton: *Search for keV-Scale Sterile Neutrinos with KATRIN.* master thesis, KIT, 2015.

[Hub16] Huber, A.: *Technical Realisation of Phase-0 keV-scale sterile neutrino search.* Presentation at the 31st KATRIN-Collaboration meeting in Karlsruhe, 2016.

[I+16] Incerti, S. *et al.*: *Simulation of Auger electron emission from nanometer-size gold targets using the Geant4 Monte Carlo simulation toolkit.* Nuclear Instruments and Methods in Physics Research Section B: Beam Interactions with Materials and Atoms, 372:91 – 101, 2016.

[K+01] Kodama, K. *et al.*: *Observation of tau neutrino interactions.* Physics Letters B, 504(3):218 – 224, 2001.

[KAT05] KATRIN Collaboration: *KATRIN design report 2004.* FZKA Scientific Report 7090, KATRIN Collaboration, 2005.

[KEHM82] Kalef-Erza, J., Y.S. Horowitz und J.M. Mack: *Electron backscattering from low Z thick absorbers.* Nuclear Instruments and Methods in Physics Research, 195(3):587 – 595, 1982.

[Kle14] Kleesiek, Marco: *A Data-Analysis and Sensitivity-Optimization Framework for the KATRIN Experiment.* dissertation, KIT, 2014. `https://publikationen.bibliothek.kit.edu/1000043301`.

[Kna17] Knapp, Felix: *Impacts of Magnetic Traps in the WGTS on a Sterile Neutrino Search with KATRIN.* Ongoing Bachelorthesis, 2017.

[M+15] Mertens, S. *et al.*: *Sensitivity of Next-Generation Tritium Beta-Decay Experiments for keV-Scale Sterile Neutrinos.* JCAP, 1502(02), 2015.

[Mer16] 2016. Personal correspondence with Susanne Mertens (MPI München).

[Pau30] Pauli, Wolfgang: *Sehr geehrte radioaktive Damen und Herren*, 1930. letter to the Gauvereins-Tagung in Tuebingen.

[Pon58] Pontecorvo, B.: *Inverse beta processes and nonconservation of lepton charge.* Sov. Phys. JETP, 7:172–173, 1958. [Zh. Eksp. Teor. Fiz.34,247(1957)].

[Rin16] 2016. Personal correspondence with Rolf Rinderspacher (IKP).